Summers et al. Fire Science Reviews (2015) 4:3
DOI 10.1186/s40038-015-0007-5

Fire Science Reviews
a SpringerOpen Journal

REVIEW Open Access

Overview of aluminum alloy mechanical properties during and after fires

Patrick T Summers[1], Yanyun Chen[2], Christian M Rippe[1], Ben Allen[2], Adrian P Mouritz[3], Scott W Case[2] and Brian Y Lattimer[1*]

Abstract

Aluminum alloys are increasingly being used in a broad spectrum of load-bearing applications such as lightweight structures, light rail, bridge decks, marine crafts, and off-shore platforms. A major concern in the design of land-based and marine aluminum structures is fire safety, at least in part due to mechanical property reduction at temperatures significantly lower than that for steel. A substantial concern also exists regarding the integrity and stability of an aluminum structure following a fire; however, little research has been reported on this topic. This paper provides a broad overview of the mechanical behavior of aluminum alloys both during and following fire. The two aluminum alloys discussed in this work, 5083-H116 and 6061-T651, were selected due to their prevalence as lightweight structural alloys and their differing strengthening mechanisms (5083 – strain hardened, 6061 – precipitation hardened). The high temperature quasi-static mechanical and creep behavior are discussed. A creep model is presented to predict the secondary and tertiary creep strains followed by creep rupture. The residual mechanical behavior following fire (with and without applied stress) is elucidated in terms of the governing kinetically-dependent microstructural mechanisms. A review is provided on modeling techniques for residual mechanical behavior following fire including empirical relations, physically-based constitutive models, and finite element implementations. The principal objective is to provide a comprehensive description of select aluminum alloys, 5083-H116 and 6061-T651, to aid design and analysis of aluminum structures during and after fire.

Keywords: Aluminum alloy; High temperature; Mechanical properties; Creep; Post-fire; Residual mechanical properties; Hardness

Introduction

Aluminum alloys are increasingly being used in a broad spectrum of load-bearing applications such as lightweight structures, light rail, bridge decks, marine crafts, and off-shore platforms. A major concern in the design of land-based and marine aluminum structures is fire safety. This concern is exacerbated for aluminum alloys due to property degradation which occurs at temperatures as low as 150°C with a 50% yield strength reduction at ~275°C (Langhelle and Amdahl 2001). As a result, special design considerations must be given to ensure structural integrity. In support of this, aluminum alloy mechanical behavior at elevated temperature has been extensively researched (Maljaars et al. 2008; Kandare et al. 2010; Clausen et al. 2004; El-Danaf et al. 2008) and design guides for structural behavior during fires have been developed (e.g., Eurocode 9 (BSI 2007)). However, limited research has been conducted on the residual mechanical behavior of aluminum following fire. This is a pertinent issue that requires consideration to effectively evaluate structural stability following a fire and assess replacement of fire damaged structural elements. Thus, analysis and design of aluminum structures requires a well-developed understanding of both the elevated temperature and residual mechanical behavior of the aluminum alloys of interest. The work presented in this paper focuses on two specific alloys: 5083-H116 and 6061-T651, which are commonly used structural alloys for lightweight applications.

High temperature thermal and mechanical property measurements have been reported in the literature for different aluminum alloys. Maljaars, et al. (2005), Mazzolani (1995), and Eurocode 9 (BSI 2007) provide an overview of

* Correspondence: lattimer@vt.edu
[1]Department of Mechanical Engineering, Virginia Tech, Blacksburg, VA 24061, USA
Full list of author information is available at the end of the article

Springer

© 2015 Summers et al.; licensee Springer. This is an Open Access article distributed under the terms of the Creative Commons Attribution License (http://creativecommons.org/licenses/by/4.0), which permits unrestricted use, distribution, and reproduction in any medium, provided the original work is properly credited.

published thermal and mechanical property data for aluminum. Creep data for some aluminum alloys is presented in (Maljaars et al. 2008; Maljaars et al. 2005; Maljaars et al. 2009a; Maljaars et al. 2009b), (Faggiano et al. 2004), and (Mazzolani 1995). Limited elevated temperature mechanical property data was provided by Amdahl, et al. (2001) for aluminum 5083-H116 and (Langhelle 1996) for 6082 with T4 and T6 heat treatments including some stress-strain curves detailing plastic deformation and the fracture strain. Aluminum alloys contain a wide range of chemical compositions and tempers, even within the same alloy family (e.g., 5xxx-series wrought aluminum alloys). Thus, the elevated temperature mechanical properties required to analyze and model the structural response must be measured for the specific aluminum alloy of interest. Note, careful consideration of alloy microstructures may allow for extrapolation of existing mechanical properties to other similar aluminum alloys.

Mechanical property degradation following an elevated temperature exposure can in part be understood through the strengthening mechanisms, which are alloy-dependent due to different chemical compositions and microstructural states from material processing (e.g., cold-work, heat treatment). 5xxx-series (Al-Mg) aluminum alloys are strain hardened alloys whose primary strengthening mechanism is by solid solution strengthening and grain refinement (Huskins et al. 2010). The primary reduction in strength is caused by recrystallization upon annealing (250 – 350°C), which destroys grain refinement (Dieter 1976). Dislocation recovery and precipitate growth at lower temperatures (150 – 250°C) also reduces strength through dislocation wall cell (subgrain) coarsening (Vandermeer and Hansen 2008) and, to a lesser extent, dilution of the Mg solid solution content in the aluminum matrix (Popović and Romhanji 2008). Recrystallization is a kinetic (time-temperature dependent) process (Doherty et al. 1997). Therefore, strength reduction is also a kinetically dependent process. 6xxx-series (Al-Mg-Si) aluminum alloys are precipitation hardened (heat treated) whose primary strengthening mechanism is through precipitate growth under controlled heating (aging) to a desired state (e.g., T6) (Dieter 1976; Edwards et al. 1998). Elevated temperature exposure causes further precipitate growth (overaging) and strength reduction (Gupta et al. 2001). Precipitate growth, and the resulting strength reduction, is also a kinetically-dependent diffusion process (Gaber et al. 2006; Aouabdia et al. 2010; Doan et al. 2000). Due to the kinetic nature of the governing strengthening mechanisms, the residual mechanical properties must be characterized considering the effects of both maximum exposure temperature and the temporal history (i.e., heating rate) to reach this temperature. Studies considering only exposure temperature are inadequate to fully understand residual mechanical behavior after fire.

Residual mechanical properties of 5xxx and 6xxx-series aluminum alloys have been quantified for specimens subjected to an isothermal exposure for different durations (Matulich 2011; Summers et al. 2012). In these studies, 5083-H116 and 6082-T651 specimens were isothermally heated (100 – 500°C) for durations up to 2 h. The primary strength reduction in both alloys occurred from 200 – 400°C, leading to decreases in yield strength of 37% and 67% for 5083-H116 and 6082-T651, respectively. The strength reduction magnitude was dependent on isothermal exposure temperature and duration. However, it was difficult to clearly discern the kinetic nature of the residual mechanical behavior due to the isothermal heating used. Thus, the ability to relate property change to microstructural evolution was limited.

Insight into the kinetic nature of aluminum residual strength following a fire may also be gained using aluminum welding research. The welding process causes spatially varying thermal histories with maximum temperatures and heating/cooling rates dependent on distance from the weld. Gallais, et al. (2007) extracted micro-tensile specimens from different zones of an 6056 friction stir weld. Lower yield stresses were measured for zones closer to the welded region; however, properties were not correlated to specific thermal histories. (Maisonnette et al. 2011) studied 6061-T6 exposed at heating rates of 30 – 1200°C/min. A significant heating rate dependence was observed. Exposure at 30 and 1200°C/min to 400°C resulted in yield strengths of 90 MPa and 170 MPa, respectively. Additional data is needed to quantify residual mechanical properties (i.e., yield strength, ultimate strength, ductility) at intermediate exposure temperatures and heating rates; specifically at refined intervals to relate to microstructural evolution.

The research overview presented in this paper provides a comprehensive description of 5083-H116 and 6061-T651 aluminum alloy mechanical behavior to aid design and analysis of aluminum structures during and after a fire. As such, the paper is organized into sections that follow the natural progression of a fire.

- Section 2: Material description.
- Section 3: High temperature material behavior, including thermal properties, quasi-static behavior and properties (e.g., Young's modulus, yield strength), and creep behavior.
- Section 4: Residual mechanical behavior after prior thermal exposure. The alloys were thermally exposed at different heating rates to elicit the kinetic nature of microstructural evolution and relate this to strength degradation. Constant, linear heating rate was employed to simulate the initial transient temperature rise during a fire, which is approximately linear (see (Suzuki et al. 2005)). The heating rates were

determined using a structural element (with and without insulation) exposed to the UL 1709 (Underwriter Laboratories 1990) standard fire exposure (see (Summers 2014) for details).

- Section 5: Residual mechanical behavior after a thermo-mechanical exposure. The effect of stress during heating (i.e., creep) is examined. Microstructural evolution and damage is related to residual mechanical behavior after fire.
- Section 6: Prediction of residual mechanical behavior after fire exposure. Models are detailed which utilize microstructural evolution to predict residual mechanical behavior using only the thermal history as input. A finite element implementation of the residual mechanical behavior analysis is implemented for a representative structural section exposed to one-sided heating.

Material description

The materials included in this study are 5083-H116 and 6061-T651. These alloys were investigated due to their prevalence as common structural alloys, especially in light-weight transportation and structural applications, and their different strengthening mechanisms. 5083 is strengthened by strain hardening (cold work). It is a weldable, moderate strength alloy which exhibits good corrosion resistance in the H116 condition. 6061 is strengthened by precipitation hardening (heat treatment). It is a weldable, high strength alloy which also exhibits good corrosion resistance. The chemical composition of the alloys are shown in Table 1.

High temperature behavior

This section on aluminum material behavior contains the high temperature mechanical behavior of 5083-H116 and 6061-T651. The presented data includes uniaxial tension (per ASTM E21 (ASTM Standard E21 2009)) and uniaxial tensile creep (per ASTM E139 (ASTM 2011)) tests performed at temperatures up to 500°C. A modified Kachanov-Rabotnov model for the creep response is also presented, including secondary and tertiary regions and creep rupture. Refer to (Allen 2012) for details regarding the high temperature mechanical tests, including specimen geometry, testing machine details, heating apparatus, and strain measurement.

The high temperature mechanical behavior data is presented to provide a comprehensive description of the high temperature response of the 5083-H116 and 6061-T651. It is hoped that such a dataset, and its associated understanding, aids design efforts with the selected, and similar, aluminum alloys.

Table 1 Chemical composition (wt%) of 5083-H116 and 6061-T651

Alloy	Si	Fe	Cu	Mn	Mg	Cr	Zn	Ti	Al
5083-H116	0.11	0.24	0.06	0.57	4.4	0.09	0.02	0.02	bal
6061-T651	0.66	0.4	0.24	0.07	0.9	0.18	0.02	0.02	bal

Thermal properties

The high temperature thermal properties are included to provide a complete description for use in analyzing and modeling the thermo-mechanical constitutive response. The thermal properties are compared to those in Eurocode 9 (BSI 2007).

The thermal diffusivity, as well as specific heat capacity, of the alloys was measured using the laser flash diffusivity method (per (ASTM Standard E1461 2013)). The thermal conductivities calculated from these measurements are shown in Figure 1. Note, alloy densities used were 5083-H116 – 2660 kg/m^3 and 6061-T651 – 2690 kg/m^3. The notably higher thermal conductivity for 6061 is the result of a lower alloying content as compared to 5083 (see Table 1). Differential scanning calorimetry (DSC) was used in addition to the laser flash method to determine the specific heat capacities (per ASTM E1269 (ASTM Standard E1269 2005)). DSC testing was performed at 20°C/min in an inert nitrogen environment. Refer to Agarwal and Lattimer (2012) for further DSC testing details. The specific heat capacities are compared against that in Eurocode 9 (BSI 2007) in Figure 2. The thermal expansion, shown in Figure 3, was measured using a thermo-mechanical analyzer (TMA). Table 2 contains the linear coefficients of thermal expansions obtained from this data.

Stress-strain relations

5083-H116 tensile engineering stress-strain relations are shown in Figure 4. Yield and ultimate strength decrease between 200 – 350°C, which is expected with increasing

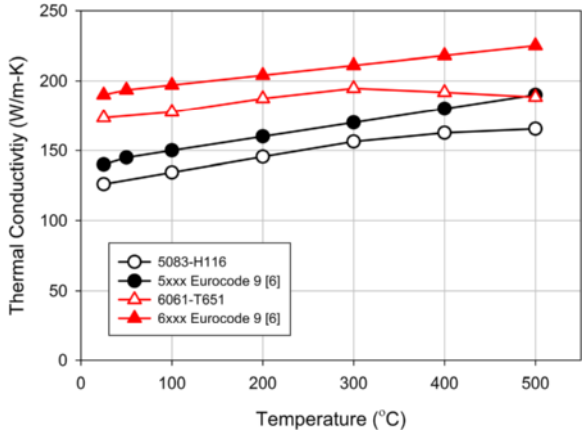

Figure 1 5083-H116 and 6061-T651 thermal conductivity obtained via laser flash diffusivity measurements (per (ASTM Standard E1461 2013)). Eurocode 9 (BSI 2007) data shown for comparison.

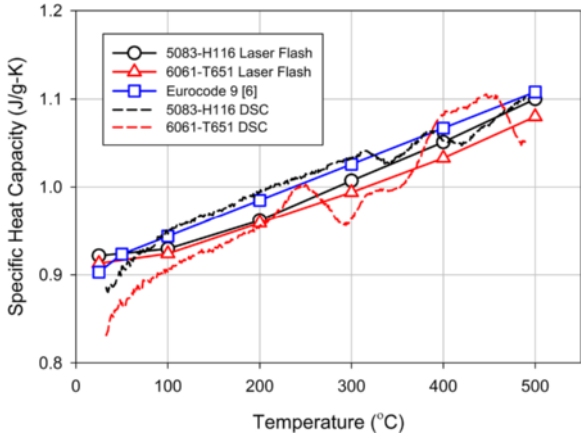

Figure 2 5083-H116 and 6061-T651 thermal conductivity obtained via laser flash diffusivity measurements (per (ASTM Standard E1461 2013)) and differential scanning calorimetry (per (ASTM Standard E1269 2005)). Eurocode 9 (BSI 2007) data shown for comparison.

temperature. Strain at failure also generally increases with temperature; however, the failure strain at 500°C reduces slightly. The necked regions after failure, shown in Figure 5, corroborates this assertion. 5083 exhibits ductile shear failure up to 100°C, after which the material transitions towards pure ductile failure at 400°C. At temperatures above 400°C, a transition to a brittle-type fracture was observed.

Elevated temperature 6061-T651 engineering stress-strain relations are shown in Figure 6. The measured mechanical behavior is similar to that for 5083-H116; however, the failure strain remains relatively constant from room-temperature to 400°C. Above 400°C, the failure strain increases significantly. This is confirmed by the increasing reduction in area at the necked region shown in Figure 7 for temperatures above 400°C. Ductile fracture is the dominant failure mode for all shown specimens.

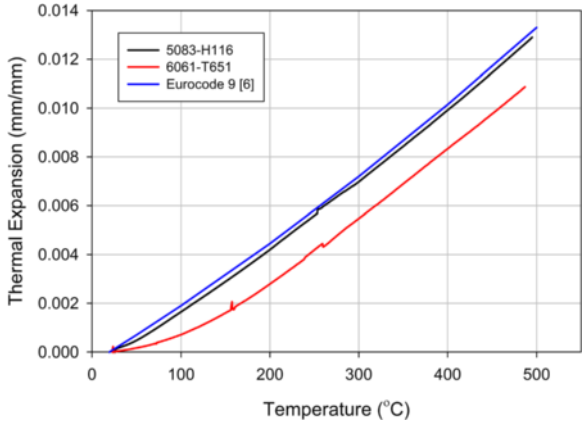

Figure 3 5083-H116 and 6061-T651 thermal expansion obtained using a thermomechanical analyzer at a heating rate of 20°C/min. Eurocode 9 (BSI 2007) data shown for comparison.

Table 2 Linear coefficients of thermal expansion (CTE) for 5083-H116, 6061-T651, and that derived from the general aluminum thermal expansion relation in Eurocode 9 (BSI 2007)

	CTE, linear (μm/m-°C)
5083-H116	27.6
6061-T651	27.9
Eurocode 9	27.4

Young's modulus

The elevated temperature 5083-H116 and 6061-T651 Young's modulus is shown in Figure 8. The error bars signify the standard deviation calculated from the stress-strain relations (three for each temperature). The Young's modulus nearly linearly decreases with increasing temperature; however, 5083-H116 deviates from this trend from about 200 – 300°C. These temperatures correspond with dislocation recovery and the onset of recrystallization (Summers et al. 2014) and are likely related to this microstructural evolution. The Young's modulus values reported in Eurocode 9 (BSI 2007) agree well with the measured data.

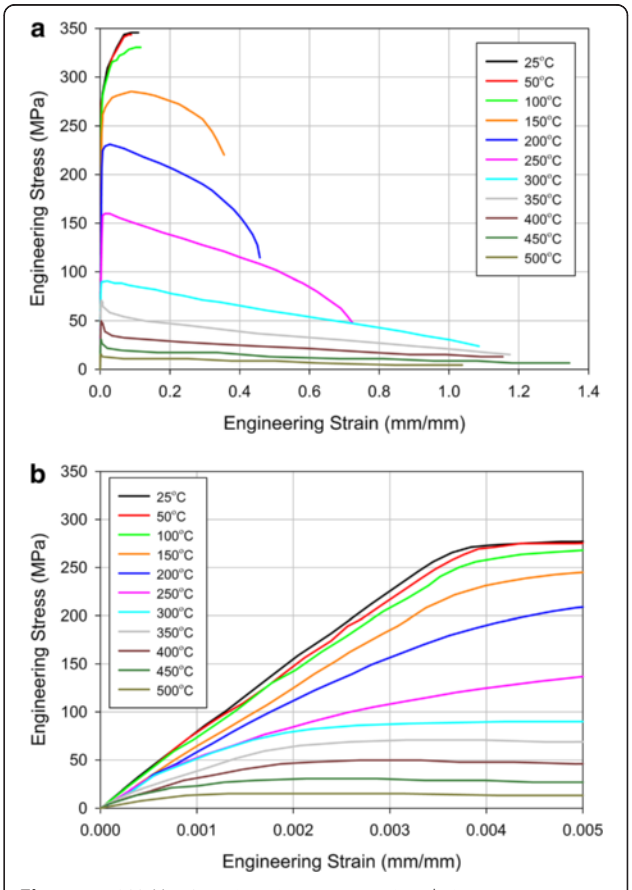

Figure 4 5083-H116 engineering stress-strain relations.

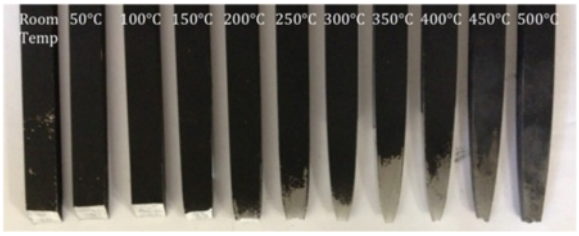

Figure 5 5083-H116 tensile specimens fracture morphology.

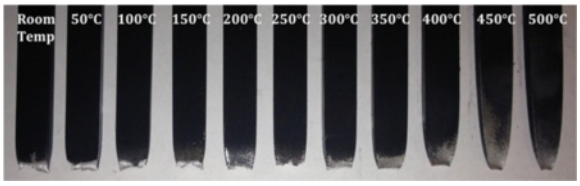

Figure 7 6061-T651 tensile specimen fracture morphology.

Yield strength

5083-H116 and 6061-T651 elevated temperature yield strengths (0.2% offset method) are shown in Figure 9. The error bars signify the standard deviation calculated from the stress-strain relations (three for each temperature). 5083-H116 yield strength remains relatively constant between room-temperature and 150°C. From about 150 – 300°C, the strength significantly decreases from about 250 to 90 MPa. Above 300°C, yield strength linearly decreases above until reaching a minimum. The yield strengths reported for 5083-H113 in Ref. (Kaufman 2000) are less than that for 5083-H116. The most notable deviation occurs from about 250 – 400°C and may be explained by different initial material states. 6061-T651 yield strength exhibits a linear decrease from room-temperature (~320 MPa) to 150°C (~240 MPa). A sigmoidal decrease occurs at higher temperature with the largest drop (~140 MPa decrease) occurring from 200 – 300°C. The yield strengths reported for similar 6061 alloys follows essentially the same trend as that measured for 6061-T651; however, the strengths are slightly reduced.

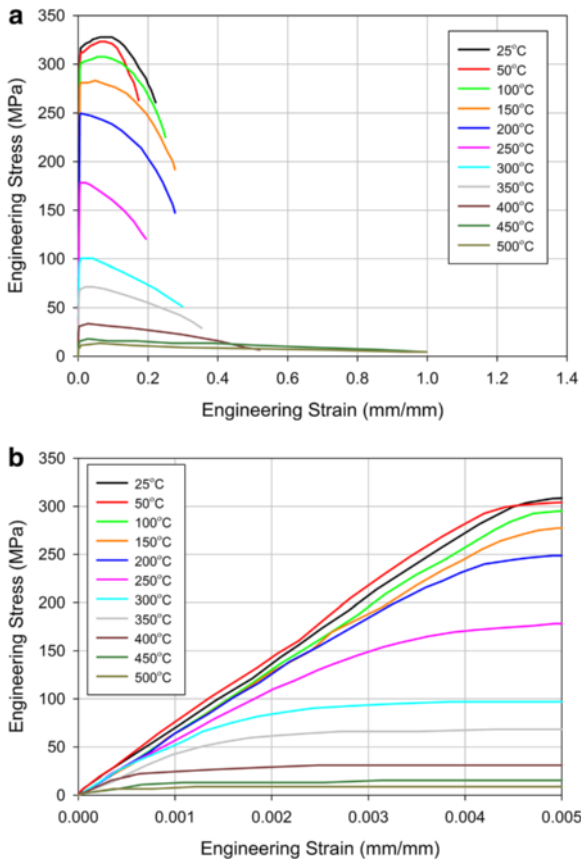

Figure 6 6061-T651 engineering stress-strain relations.

Ultimate strength

5083-H116 and 6061-T651 elevated temperature ultimate strengths are shown in Figure 10. The error bars signify the standard deviation calculated from the stress-strain relations (three for each temperature). Both alloys exhibit trends in decreasing ultimate strength which are similar to that previously shown for yield strength (Figure 9). The ultimate strengths are generally reached at very low strains as shown in stress-strain relations for 5083 (Figure 4) and 6061 (Figure 6). Above 200°C, the ultimate strength is reached at strains not much higher than that at yield. The ultimate strengths reported for similar 5083 and 6061 alloys, i.e., 5083-H113 and 6061-T6 in Ref. (Kaufman 2000), are essentially the same as that measured for the alloys in this work.

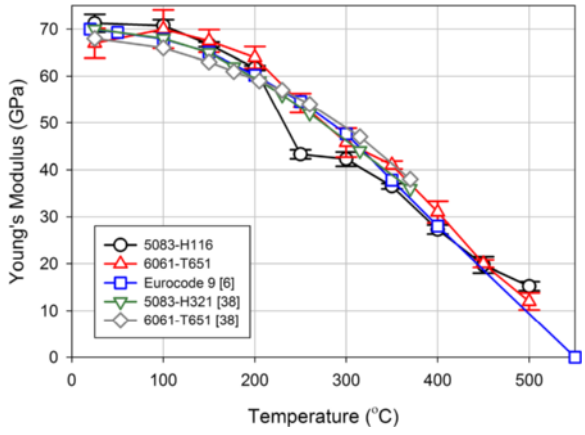

Figure 8 5083-H116 and 6061-T651 elevated temperature Young's modulus. Data reported in Eurocode 9 (BSI 2007) and by (Kaufman 2000) is shown for comparison.

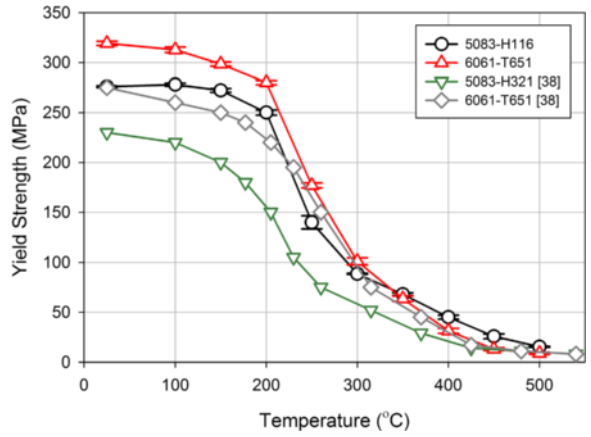

Figure 9 5083-H116 and 6061-T651 elevated temperature yield strengths (0.2% offset method). Data reported in (Kaufman 2000) is shown for comparison.

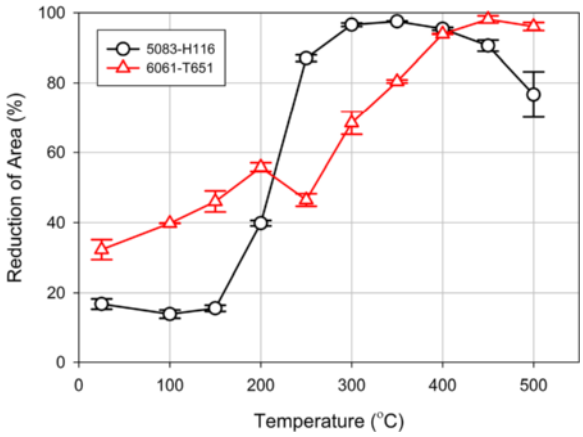

Figure 11 5083-H116 and 6061-T651 reduction in area after failure during tension testing at elevated temperatures (Allen 2012).

Ductility

The reduction in area data measured after failure of 5083-H116 and 6061-T651 are shown as a function of temperature in Figure 11. The error bars signify the standard deviation calculated from the stress-strain relations (three for each temperature). 5083 remains relatively constant until 100°C at which point the reduction in area significantly increases from ~15% to ~95% at 300°C. It then decreases slightly with increasing temperature to ~75% at 500°C. The reduction in area evolution is reflected by the failed samples shown in Figure 5. The reduction in area for 6061 increases linearly from ~30% at room-temperature to ~95% at 400°C; however, a notable decrease was measured at 250°C. This approximately corresponds to temperatures at which the primary strengthening phase undergoes significant evolution (Summers et al. 2014). The reduction in area remains relatively constant above 400°C.

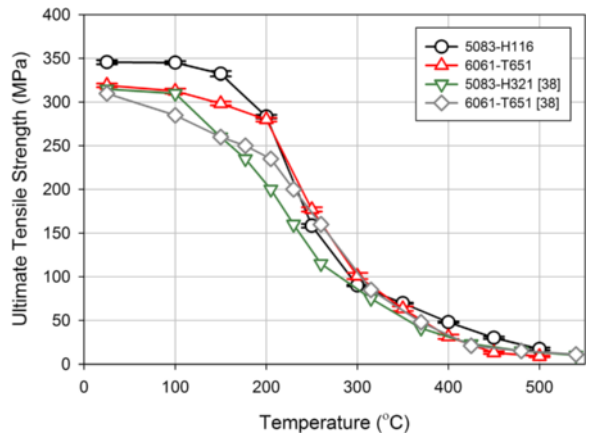

Figure 10 5083-H116 and 6061-T651 elevated temperature ultimate strengths. Data reported in (Kaufmann et al. 1999) is shown for comparison.

Creep

Thermo-mechanical creep and rupture of aluminum alloys are important considerations due to aluminum's relatively low melting temperature (~660°C for pure Al with alloying additions lower the melting temperature). Uniaxial tensile creep (constant stress and temperature) tests were performed by Allen (Allen 2012) (per ASTM E139 (ASTM 2011)). The test temperatures ranged from 200 – 400°C. Tests were not conducted at temperatures below 200°C as creep strains are typically not considered significant at temperatures below ~40 – 50% the absolute melting temperature (Courtney 2000); this is ~100 – 180°C for the alloys in this work. The applied constant stresses ranged from about 40 – 90% of the measured yield strengths at the respective temperatures. For each temperature and stress combination, multiple tests were conducted. Refer to Allen (Allen 2012) for further details regarding specimen geometry, mechanical testing machine, heating apparatus, and strain measurement. Constitutive models for the creep behavior of both alloys were also derived from the presented data.

Creep behavior

The creep behavior of 5083-H116 from Allen (2012) is shown in Figure 12. Note, a select representative creep curve is shown of several replicates performed at each temperature-stress condition. A small primary creep region exists for exposures below 250°C; however, negligible primary creep exists at higher temperatures. The secondary (steady-state) creep duration is large for all cases with the tertiary region increasing with duration and temperature.

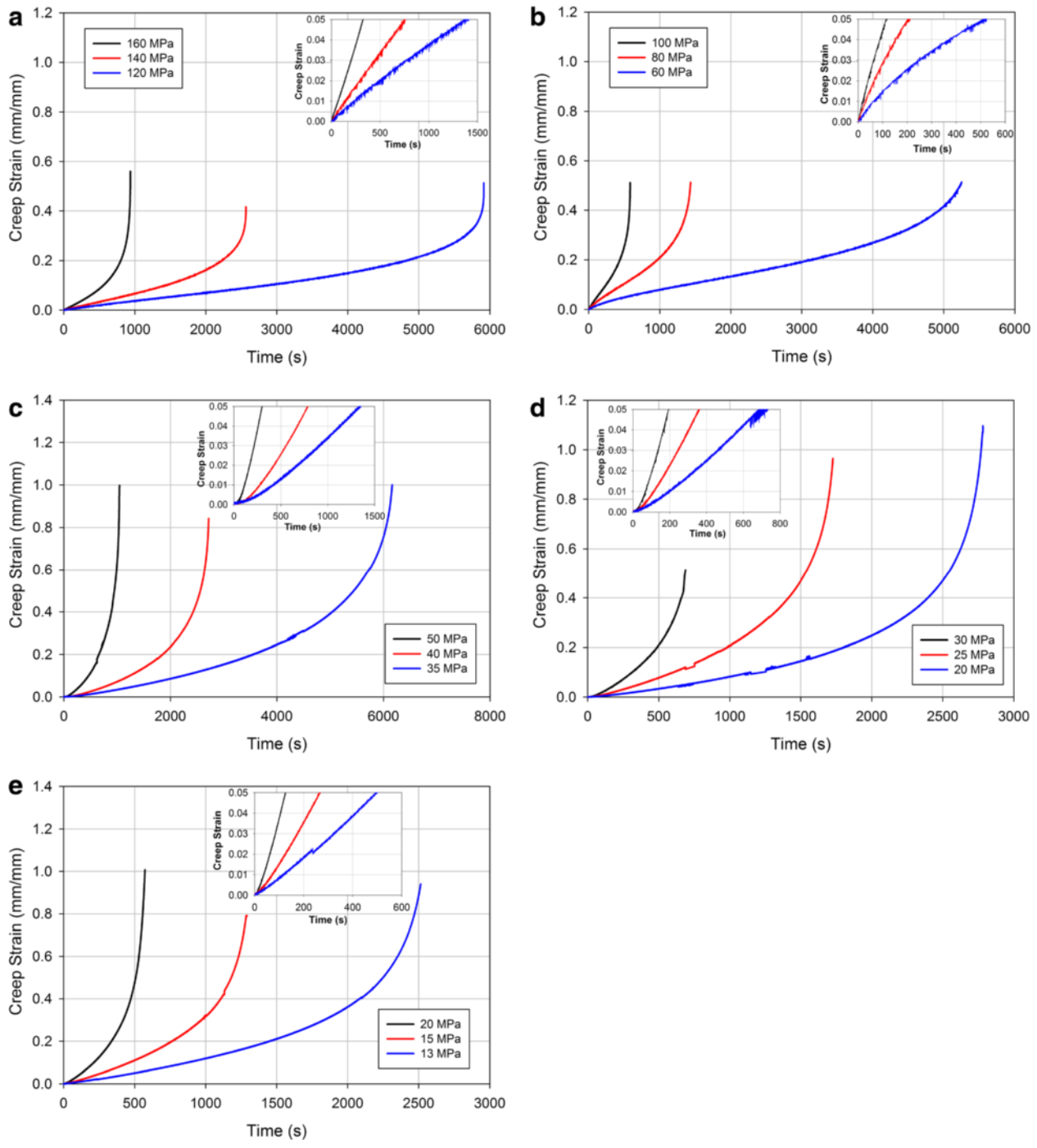

Figure 12 5083-H116 creep behavior at **(a)** 200°C, **(b)** 250°C, **(c)** 300°C, **(d)** 350°C, and **(e)** 400°C. The inset figures detail the creep behavior at strains less than 5%.

The creep rupture strain exhibits a similar trend as that for quasi-static ductility (see the reduction of area measurements in Figure 11). Lower temperatures (less than ~250°C) result in lower creep rupture strains (~60%) compared to that at higher temperatures (~100%).

The creep behavior of 6061-T651 from Allen (2012) is shown in Figure 13. Note, a select representative creep curve is shown of several replicates performed at each temperature-stress condition. Similar to 5083, this alloy has a limited primary creep region which is only measured

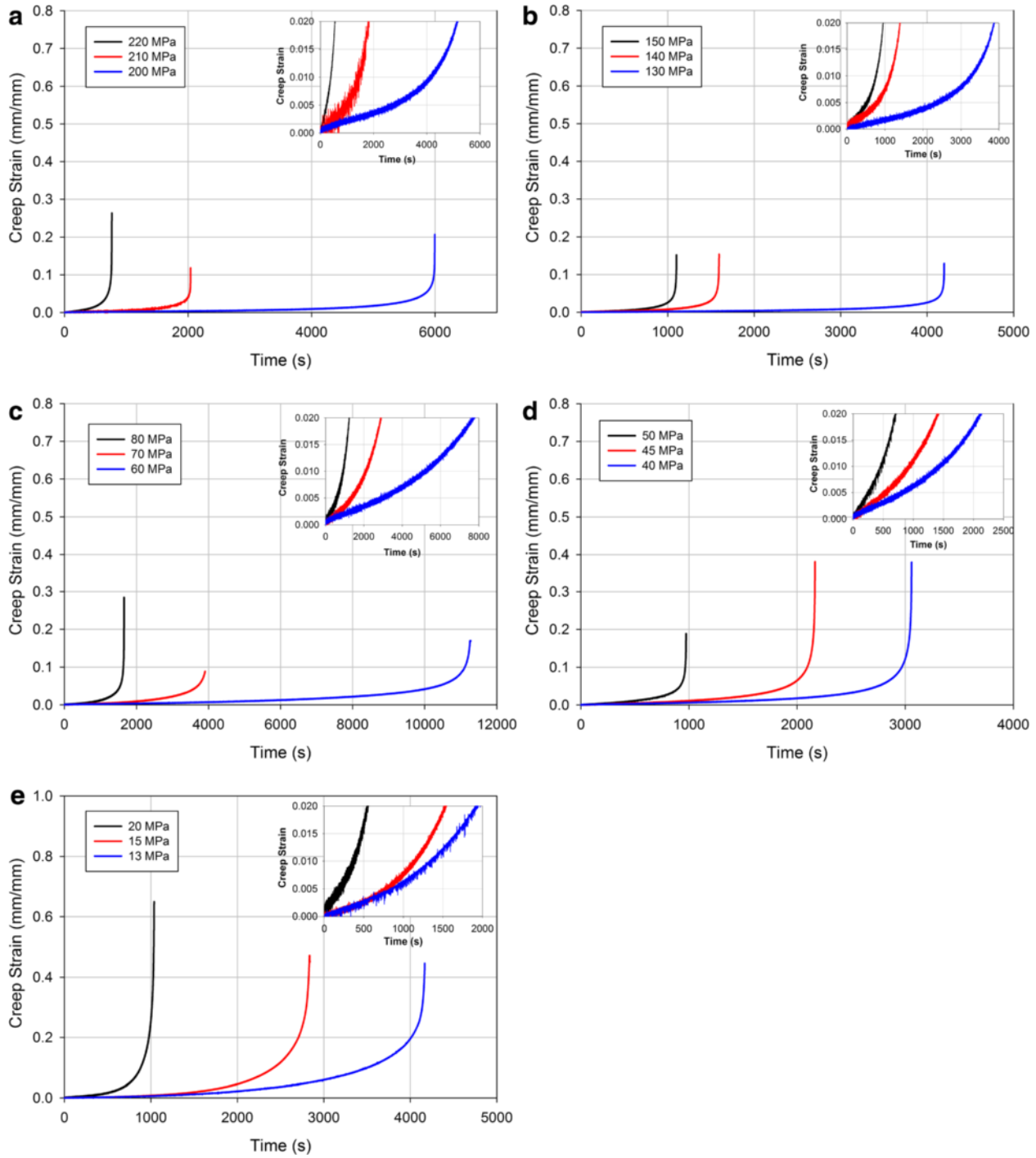

Figure 13 Creep behavior of 6061-T651 at **(a)** 200°C **(b)** 250°C **(c)** 300°C **(d)** 350°C **(e)** 400°C. The inset figures detail the creep behavior at strains less than 2%.

at 200°C for the lowest applied stress. The trends in the secondary and tertiary creep regions exhibited by 5083 are also followed by 6061; however, the secondary creep rate in 6061 is notably lower. The ductility also follows a similar behavior; creep rupture strain increases from ~20% at 200°C to ~50% at 400°C.

Creep laws

The creep response was modeled using a modified Kachanov-Rabotnov creep law. This creep law is applicable to materials that exhibit an insignificant primary creep region and is defined by three distinct parts: the secondary creep rate, the creep rupture strain, and the creep rupture

time. The secondary creep rate was modeled using a hyperbolic-sine law of the following form

$$\dot{\varepsilon}_{II} = A[\sinh(B\sigma)]^n \exp(-Q/RT) \quad (1)$$

where $\dot{\varepsilon}_{II}$ is the secondary (steady-state) creep rate (s^{-1}), A (s^{-1}), B (MPa^{-1}), and n (-) are fitting constants, Q is the activation energy (kJ/mol), R is the universal gas constant (8314 kJ/mol-K), and σ and T are the current stress (MPa) and temperature (K), respectively. Non-linear regression was used to calculate the fitting constants and activation energy using all of the experimental creep results (5083 – Figure 12, 6061 – Figure 13). The regression results are shown in Table 3. A comparison of the experimentally measured secondary creep rates measured by Allen (2012) and that predicted by the hyperbolic-sine law is shown in Figure 14. Maljaars et al. (2008) measured the creep activation energy for 5083-H111 and 6060-T66 to be 152 kJ/mol and 195 kJ/mol, respectively, using a stepwise temperature experiment. These values reasonably agree with those listed in Table 3 for 5083-H116 and 6061-T651. The differences may be attributed to the alloys used.

The tertiary creep behavior was modeled using a Kachanov based damage model (Kachanov 1999). In the traditional form, Rabotnov (1969) implemented the Kachanov damage model as a multiplicative damage term with a power-law steady-state creep law to capture unstable tertiary creep. Thus, the Kachanov-Rabotnov (K-R) creep model defines the instantaneous creep strain rate as

$$\dot{\varepsilon}_{II} = \frac{A\sigma^n}{(1-\omega)^m} \quad (2)$$

where the numerator is the power-law creep law and denominator is the damage term. The traditional K-R model was modified, replacing power-law creep with the hyperbolic-sine creep law defined in Eq. (1). Thus, the instantaneous creep strain rate becomes

$$\dot{\varepsilon} = \frac{\dot{\varepsilon}_{II}}{(1-\omega)^m} \quad (3)$$

where $\dot{\varepsilon}_{II}$ is defined in Eq. (1), ω is a damage progress parameter where $\omega = 1$ at creep rupture (-), and m is a fitting exponent (-).The evolution of the damage parameter, ω, must be known in order to solve for the instantaneous creep rate. This relationship is defined by the Kachanov damage model (Kachanov 1999). The rate of change in the damage parameter is defined as

$$\dot{\omega} = \frac{B\sigma^\nu}{(1-\omega)^\eta} \quad (4)$$

for any given stress level where B (1/MPa), ν (-), and η (-) are fitting parameters. An explicit relation for the time evolution of the damage parameter is necessary in order to determine creep strain as a function of time using Eq. (3). Thus, the damage parameter is determined from Eq. (4) using separation of variables as

$$\omega = 1-[1-(1+\eta)B\sigma^\nu t]^{\frac{1}{\eta+1}} \quad (5)$$

where t is time (s). This relation may be defined in terms of the rupture time (t_r) using the condition that $\omega = 1$ at $t = t_r$. Applying this condition to Eq. (5) results in an explicit form of the damage parameter

Table 3 Hyperbolic-sine law parameters to predict 5083-H116 and 6061-T651 secondary creep rate

Parameter	5083-H116	6061-T651
A (s^{-1})	3.69×10^{9}	2.91×10^{11}
B (Mpa^{-1})	0.0103	0.0404
n	3.55	1.74
Q (kJ/mol)	133	204

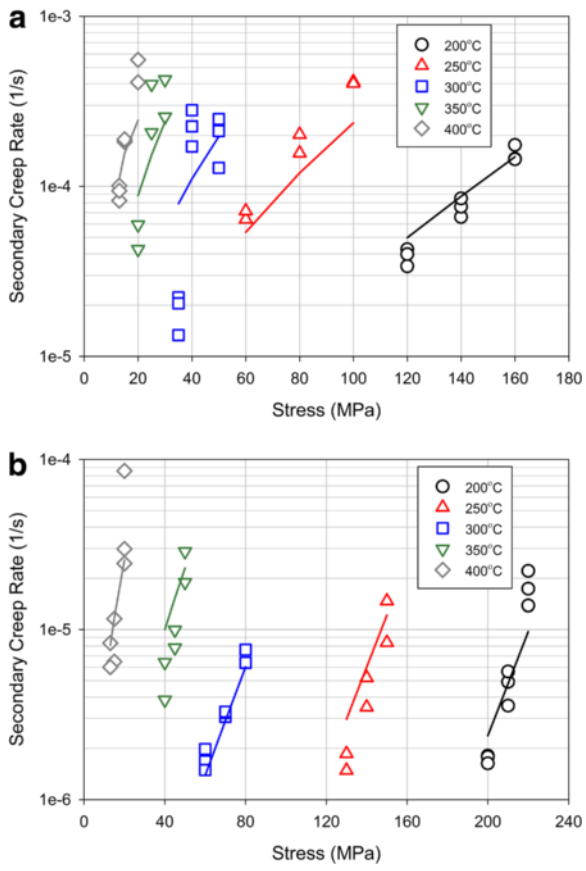

Figure 14 Comparison of experimentally measured secondary creep rates (symbols) and hyperbolic-sine secondary creep law (lines) for **(a)** 5083-H116 and **(b)** 6061-T651.

$$\omega = 1 - \left(1 - \frac{t}{t_r}\right)^{\frac{1}{\eta+1}} \quad (6)$$

Inserting Eq. (6) into Eq. (3) results in the instantaneous creep rate as a function of time as

$$\dot{\varepsilon} = \frac{\dot{\varepsilon}_{II}}{\left(1 - \frac{t}{t_r}\right)^{\frac{m}{\eta+1}}} \quad (7)$$

The instantaneous creep strain is thus defined as

$$\varepsilon = \dot{\varepsilon}_{II} t_r \lambda \left[1 - (1 - t/t_r)^{1/\lambda}\right] where \lambda = \frac{\eta + 1}{-m + \eta + 1} \quad (8)$$

where λ is a fitting constant. An explicit expression for λ was obtained using the condition of creep strain (ε) equals the creep rupture strain (ε_r) at the rupture time (t_r) as

$$\lambda = \frac{\varepsilon_r}{\dot{\varepsilon}_{II}\, t_r} \quad (9)$$

λ was calculated using the above relation for each tested temperature-stress combination resulting in average values of 3.3 and 17.7 for 5083-H116 and 6061-T651, respectively.

Creep rupture time (t_r) is the final parameter requiring a predictive relation for use in the modified K-R model. The Larson-Miller parameter (LMP), which is independent of temperature and solely a function of stress (Larson 1952), was used to model creep rupture time. A master LMP curve may be generated using isothermal, constant-load uniaxial creep tests. Thus, creep rupture time is defined as a function of the LMP as

$$t_r = 10^{\frac{LMP}{T} - C} \quad (10)$$

where LMP (K) is the Larson-Miller parameter and C (-) is material constant commonly defined as 19 or 21 for aluminum alloys. Note, despite the LMP having units of Kelvin, it is a non-physical parameter with no temperature related definition. This relation is applicable for any arbitrary temperature-stress combination. Master Larson-Miller curves were generated for both alloys using the high temperature data from Allen (2012) as well as lower temperature creep rupture data from Kaufman (2000). For 5083-H116, the supplementary data from Kaufman is for a slightly different alloy (5083-H321); therefore, some discrepancy is expected. For 6061, the supplemental data is for an identical alloy. Additional 6061 creep tests were conducted at stresses between 3 and 6 MPa at temperatures up to 550°C. Non-linear least squares regression was used to produce an analytical fit of the creep rupture data in the form

$$LMP = D \sinh(E + F\sigma^n) + G \quad (11)$$

where D (K), E (-), F (1/MPa^m), G (K), and n (-) are fitting parameters. The regression analysis results are given in Table 4. A comparison of the experimentally measured and predicted LMP is shown in Figure 15. The analytical fit represents the experimental data well for both alloys.

The LMP is integrated in the modified K-M model by substituting Eq. (10) into Eq. (8) thus obtaining the final creep strain relation as

$$\varepsilon = \dot{\varepsilon}_{II} 10^{\frac{LMP}{T} - C} \lambda \left[1 - \left(1 - \frac{t}{10^{\frac{LMP}{T} - C}}\right)^{1/\lambda}\right] \quad (12)$$

Predictions of the creep curves, including tertiary response and rupture, from Allen (5083-H116 – Figure 16, 6061-T651 – Figure 17) were calculated using this relation and the parameters in Table 3 and Table 4.

5083-H116 modified K-R creep model predictions are compared against experimental data in Figure 16. Note, the predicted creep curves terminate when creep rupture is predicted. The model captures the general trends of the creep curves as well as the shape of the tertiary region. The predicted and experimental secondary creep rates show reasonable agreement. The most pronounced error associated with the modified K-R model prediction is that for rupture time, which results in elongation and contraction of the creep curve with respect to time. This is at least partially explained by the power-law relationship between LMP and rupture time (see Eq. (10)). Thus, prediction of the tertiary region is highly sensitive to errors in the LMP. Due to this, rupture strain predictions are generally higher than experiment. Note, the character of the curve remains the same with good prediction of the secondary creep rate maintained. Also, the rupture strain prediction at 400°C (Figure 16c) may be inaccurate in part due to an assumed constant λ in the K-R model. The high ductility at this temperature makes it difficult to determine the exact point of creep rupture.

6061-T651 modified K-R creep model predictions are compared against experiment in Figure 17. As with 5083, the model captures the general behavior of the measured creep response, including the character of the

Table 4 Larson-Miller parameter fitting parameters for 5083-H116 and 6061-T651

Parameter	5083-H116	6061-T651
D (K)	-1060	-859
E (-)	-4.40	-3.60
F (1/MPa)	1.07	0.619
n (-)	0.319	0.402
G (K)	11600	12850

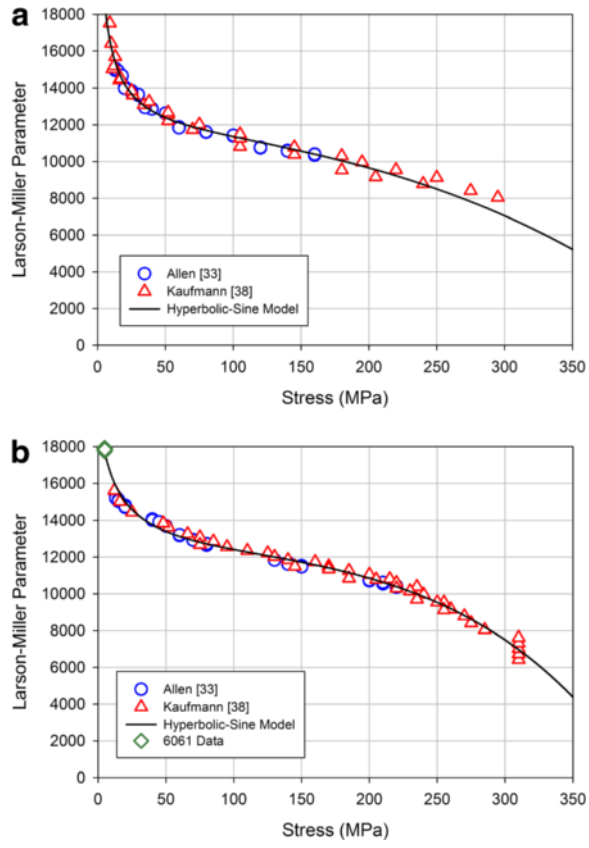

Figure 15 Experimentally determined Larson-Miller Parameters and analytical regressions for **(a)** 5083-H116 and **(b)** 6061-T651.

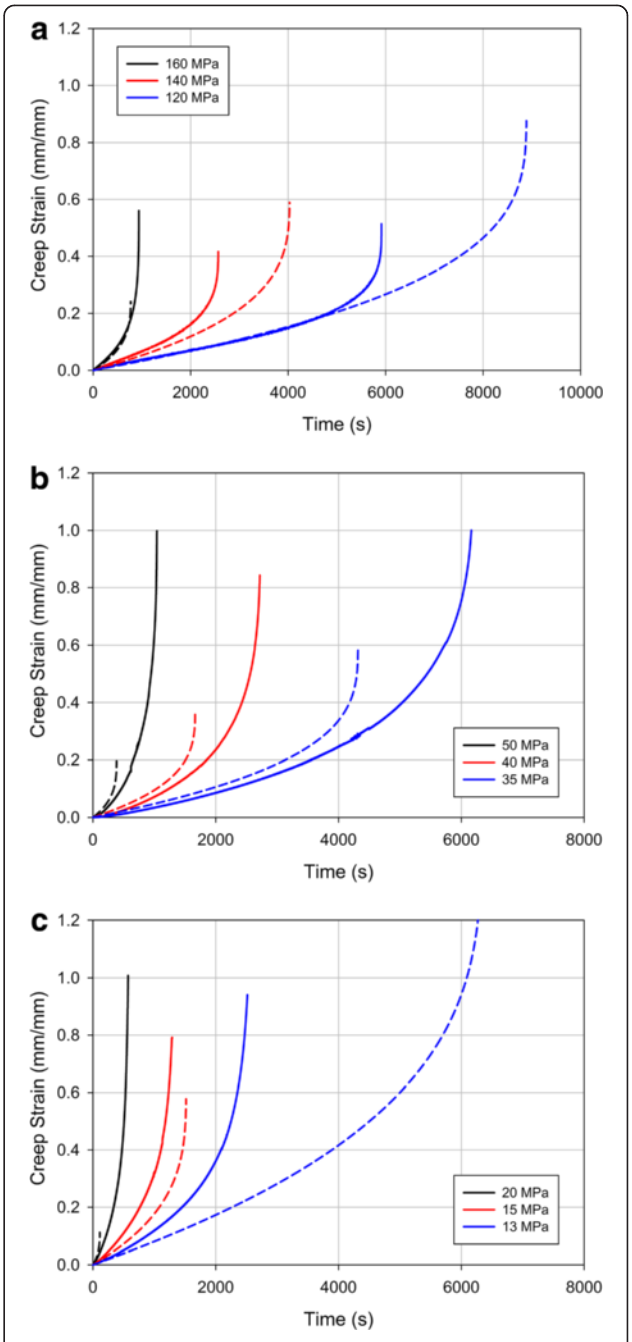

Figure 16 5083-H116 creep behavior prediction (dashed lines) using a modified Kachanov-Rabotnov model compared against experimental data (solid lines) at **(a)** 200°C, **(b)** 300°C, and **(c)** 400°C. The rupture strain is predicted as the termination of the predicted creep curves.

tertiary region. The errors in predicted creep rupture time are explained similarly to that for 5083.

Residual mechanical behavior – thermal damage only

Aluminum structural integrity after a fire is also a major concern as the residual mechanical behavior may be severely degraded as compared to the as-received material. However, limited research has been undertaken to characterize the residual strength following fire (Matulich 2011; Summers et al. 2012; Summers 2014; Summers et al. 2014). Such an understanding is necessary to effectively evaluate structural integrity and assess structural elements for replacement.

In this section, the residual mechanical behavior of 5083-H116 and 6061-T651 after simulated fire exposures is presented. The experimental study by Summers et al. (2014) is utilized to elucidate the detailed evolution and kinetic-dependence of aluminum alloy residual mechanical behavior. The residual mechanical behavior was characterized as a function of temperature and heating rate, specifically those expected during fire. Uniaxial tension tests were used to quantify the residual mechanical behavior at ambient conditions for specimens previously exposed to 100 – 500°C at heating rates of 5 – 250°C/min. The residual strength degradation mechanisms are discussed in terms of the alloy microstructural evolution. Refer to (Summers et al. 2014) for details regarding specimen geometry, testing machine details, heating apparatus, and strain measurement.

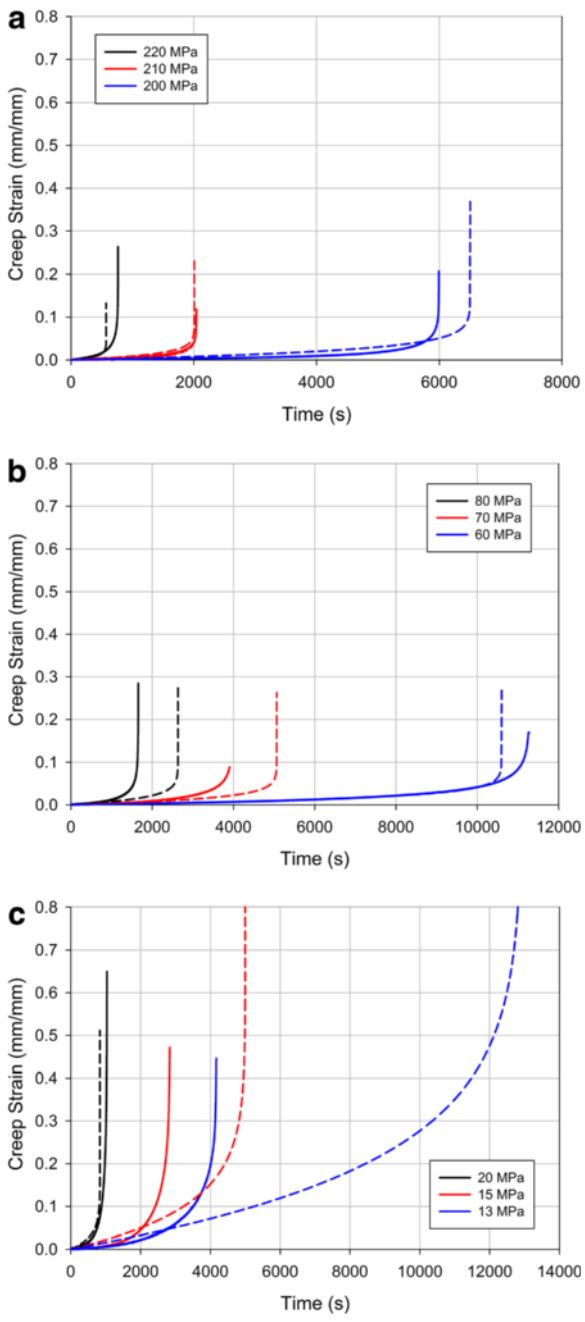

Figure 17 6061-T651 creep behavior prediction (dashed lines) using a modified Kachanov-Rabotnov model compared against experimental data (solid lines) at **(a)** 200°C, **(b)** 300°C, and **(c)** 400°C. The rupture strain is predicted as the termination of the predicted creep curves.

The elevated temperature exposure used to simulate various possible fire conditions, and its effect on residual mechanical properties, are as follows. A constant, linear heating rate to prescribed temperatures was used followed by immediate water quenching. Water quenching was used, rather than air cooling, to isolate the factors governing time-temperature dependent material evolution. This constant heating rate is an analog for the initial transient temperature increase during a fire (see the representative time-temperature curves in Ref. (Suzuki et al. 2005)). Refer to Summers (2014) for further details, including the method by which the heating rates were determined using a standard structural element (with and without insulation) exposed to a UL 1709 (Underwriter Laboratories 1990) standard fire exposure.

Experimental results

Stress-strain relations

The residual stress-strain behavior of 5083-H116 and 6061-T651 after heating at 20°C/min are shown in Figure 18. 5083 (Figure 18a) exhibits significant strain hardening in the as-received state which also increases considerably with increasing prior exposure temperature. The observed stress stepping behavior is caused by serrated yielding, also known as the Portevin-Le Chatelier (PLC) effect (Wen and Morris 2003). This behavior is common in solid solution hardened and cold worked aluminum alloys, such as 5083. The strain at ultimate strength increases above ~300°C for 5083. 6061 (Figure 16b) exhibits a nearly linear decrease in strain at ultimate strength from 200 – 300°C; strains then increase to the as-received value at 400°C. The work hardening rate ($d\sigma/d\varepsilon$) also changes with increasing temperature, indicating the microstructural mechanisms governing mechanical behavior undergo significant evolution from the as-received state. The hardening capacity (stress change from yield strength to ultimate strength) increases significantly with temperature for both alloys.

Plastic flow characteristics

The residual work hardening rates ($d\sigma/d\varepsilon$) are shown in Figure 19. The hardening rates were calculated using a moving window polynomial fit of the true stress-logarithmic strain relations of specimens previously heated at 20°C/min (Summers et al. 2014). 5083 required additional smoothing by considering only the maxima occurring during serrations in the σ-ε relations (Verdier et al. 1998a).

5083 experiences a steady increase in $d\sigma/d\varepsilon$ at equivalent flow stresses ($\sigma - \sigma_{0.2\%}$) with increasing temperature up to 300°C. A more rapid increase is observed with an increase in temperature from 300°C to 330°C, at which point $d\sigma/d\varepsilon$ remains unchanged with further increasing temperature.

6061 experiences an increase in $d\sigma/d\varepsilon$ at equivalent flow stresses and a change in slope with increasing temperature. Minor work hardening occurs below 200°C as indicated by the low values of $d\sigma/d\varepsilon$ and relatively low strains at ultimate strength. The value of $d\sigma/d\varepsilon$ also approaches zero slope rapidly after yield. At 300°C, the material exhibited an increase in slope, indicating a higher work hardening capacity. Further increase in temperature to 350°C results in a significant increase in $d\sigma/d\varepsilon$ and its slope. This is indicative

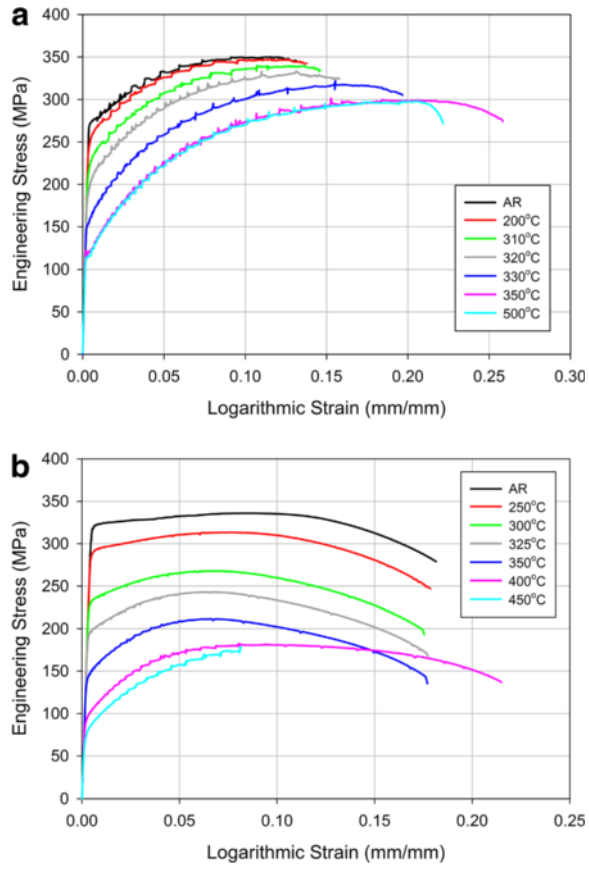

Figure 18 Engineering stress-logarithmic strain relations of **(a)** 5083-H116 and **(b)** 6061-T651 measured using DIC after exposure at 20°C/min.

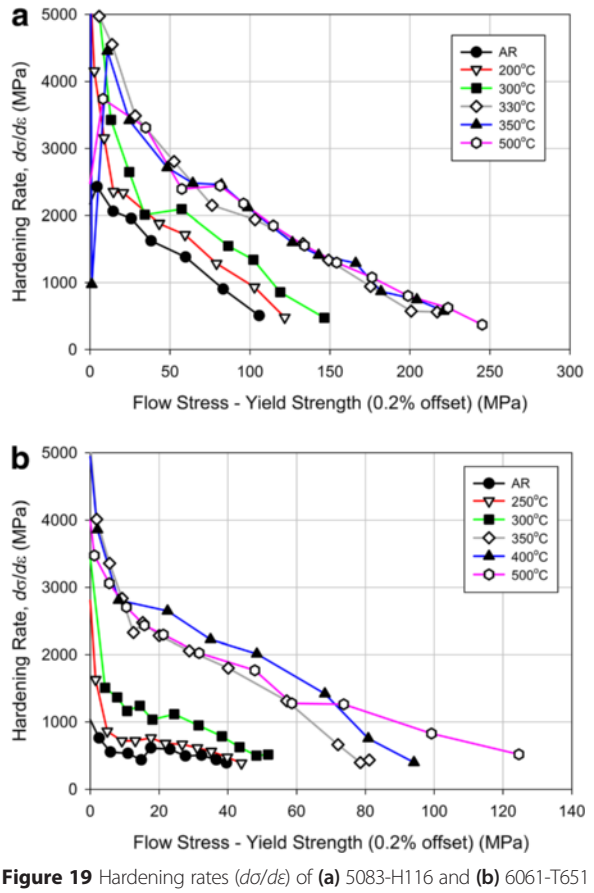

Figure 19 Hardening rates ($d\sigma/d\varepsilon$) of **(a)** 5083-H116 and **(b)** 6061-T651 calculated from the true stress-logarithmic DIC strain relations for specimens previously exposed at 20°C/min.

of a substantial increase in the work hardening capacity of the alloy. Above this temperature, the hardening rate versus equivalent flow stress is similar.

Young's modulus

The residual Young's modulus was calculated from the stress-strain relations measured using strain gages. 6061 Young's modulus is nearly constant for all temperatures with an as-received value of 69.5 ± 0.2 GPa and an average for all tested temperatures is 69.4 GPa ± 0.5 GPa. 5083 exhibited a 2% increase in modulus from as-received to 300°C; however, it reverted to the as-received value above 350°C. The as-received 5083 Young's modulus is 69.6 ± 0.3 GPa and the average for all tested temperatures is 70.9 GPa ± 1.1 GPa.

Yield strength

Yield strengths were calculated using the 0.2% strain offset method. The residual yield strengths after different heating rates are shown in Figure 20 to highlight the time-temperature dependence of the mechanical behavior.

The yield strengths are reduced at relatively low temperature exposures, 150°C and 200°C for 5083 and 6061, respectively. 5083 (Figure 20a) experiences an initial 40 MPa reduction in yield strength (up to about 300°C). A minor heating rate dependence is exhibited at these temperatures (Figure 20a). The primary 5083 yield strength reduction (~100 MPa) occurs over a relatively narrow temperature range (~50°C). This reduction is significantly time-temperature dependent. For example, prior heating to 320°C at 5, 25, and 250°C/min results in residual yield strengths of 132, 207, and 235 MPa, respectively; a range of 103 MPa. The primary yield strength reduction initiates from about 280 – 320°C depending on heating rate. It also begins at about the same stress level despite different initiation temperatures. 5083 reaches the same minimum yield strength (~120 MPa) regardless of heating rate.

6061 (Figure 20b) exhibits a relatively linear yield strength reduction from 200 – 450°C. An increase in yield strength is observed after exposure to 500°C. The largest heating rate (time-temperature) dependence occurs after exposure at 350°C, having a 74 MPa difference

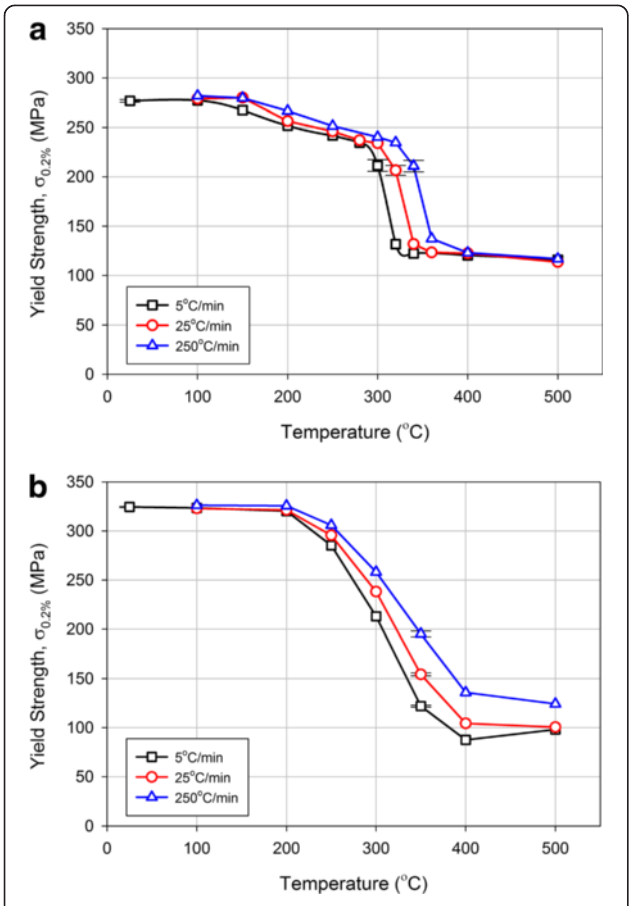

Figure 20 Yield strength (0.2% offset) of **(a)** 5083-H116 and **(b)** 6061-T651 after prior exposure at different heating rates.

between 5 and 250°C/min. The minimum yield strengths are also heating rate dependent. The yield strengths at 400°C are 87, 104, and 136 MPa for 5, 25, and 250°C/min, respectively.

Ultimate strength

The residual ultimate strength was determined in terms of true stress is given in Figure 21. 5083 ultimate strength remains nearly constant up to 500°C. A slight reduction (~40 MPa) occurs above 300°C which parallels the primary yield strength reduction shown in Figure 20. The minor reduction indicates that the mechanisms governing work hardening are relatively unaffected by elevated temperature exposure. 5083 ultimate strength is significantly dependent on heating rate over the temperature range associated with primary reduction in properties (initiating at 280 – 320°C, depending on heating rate). However, the heating rate sensitivity in this case is considered minor due to nearly negligible reduction in ultimate strength. 6061 experiences a significant reduction in ultimate strength after prior elevated temperature exposure above 200°C. The reduction is similar to that for yield

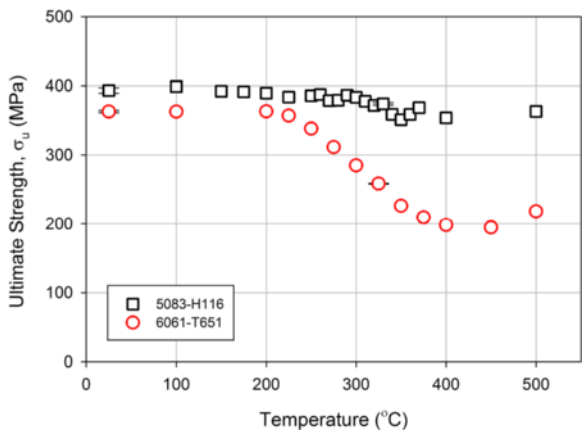

Figure 21 Ultimate strength of 5083-H116 and 6061-T651 measured after exposure at 20°C/min.

strength, indicating the governing mechanisms are likely the same. The ultimate strength also exhibits significant time-temperature dependent above 200°C.

Ductility

The ductility of 5083-H116 and 6061-T651 was analyzed in terms of reduction of area (%RA) and fracture strain in Figure 22. A distinct increase in fracture strain and %RA was measured for 5083 at temperatures above 300°C coinciding with reductions in yield and ultimate strength. Fracture strain and %RA are nearly constant below 300°C. 6061 fracture strain and %RA do not follow similar trends. Fracture strain remains nearly constant at ~0.18 to 400°C followed by a decrease to ~0.10. The %RA increases starting at 250°C (47% to 65%) followed by a drop to 55%. Prior heating above 400°C results in a significant decrease in fracture strain and %RA. Though not shown, the time-temperature dependence of ductility is similar to that observed for yield strength. 5083 is primarily dependent over a narrow 50°C range starting at 280 – 320°C depending on heating rate. 6061 exhibits significant dependence at temperatures greater than 200°C.

Discussion

The described tensile tests demonstrate that residual mechanical behavior is sensitive to both prior exposure temperature and heating rate. For accurate prediction of residual mechanical properties following a fire exposure, the time-temperature material history must be considered and not simply the maximum temperature. Less accurate results can be obtained using a maximum temperature estimate. Methods for implementing these results using a given temperature or temperature history are provided in Residual Mechanical Behavior Prediction section.

The alloys investigated exhibit exceedingly different evolutions in residual properties. This is expected as the

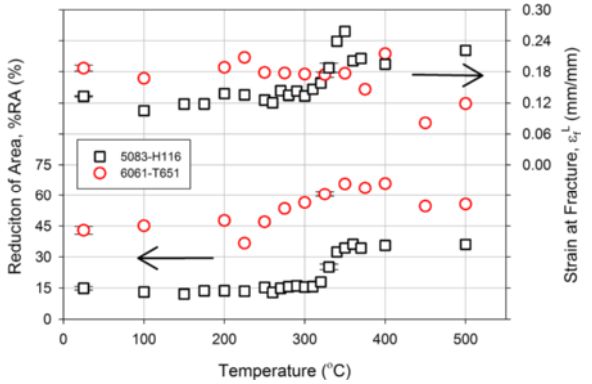

Figure 22 5083-H116 and 6061-T651 fracture strain and reduction of area after exposure at 20°C/min.

residual mechanical behavior is governed by the relative state and evolution of the microstructural strengthening mechanisms, which are discussed in detail by (Summers 2014). The primary evolving strengthening mechanisms are the grain structure in 5083-H116 and precipitates in 6061-T651. These mechanisms are developed during material processing, i.e., strain hardening (5083) and precipitation hardening (6061), to a state resulting in the desired mechanical properties. Further evolution of these mechanisms at elevated temperatures governs residual mechanical behavior.

5083-H116 mechanical properties

5083-H116 undergoes two stages of property degradation (see Figure 20a). A slight yield strength reduction occurs from about 150 – 280°C. This reduction exhibits a minor heating rate dependence most notable at ~200°C. The microstructural mechanism governing this reduction is static dislocation recovery. This microstructural process reduces subgrain strengthening due to coarsening of the as-received dislocation cell (subgrain) structure, which is shown in Figure 23. The mechanisms and details of 5083 subgrain strengthening, and its reduction during recovery, are discussed in further detail by (Summers 2014).

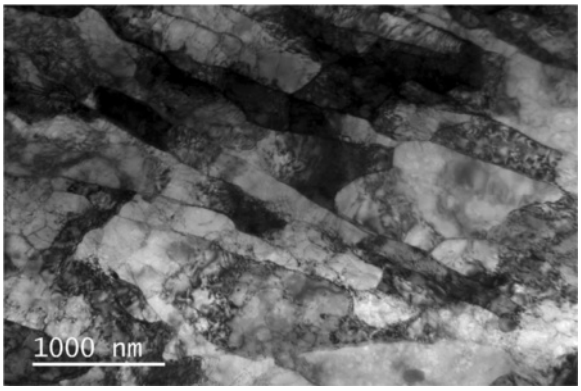

Figure 23 5083-H116 dislocation cell (subgrain) structure in the as-received state.

The primary evolution in mechanical behavior occurs from about 280 – 360°C; the specific temperature range depends on heating rate. The residual mechanical properties, including yield strength (Figure 20a), $d\sigma/d\varepsilon$ (Figure 19a), and ductility (Figure 22), are affected significantly. The ultimate strength (Figure 21a) is affected to a lesser extent. Grain recrystallization governs this reduction.

Recrystallization is the formation of an equiaxed grain structure in a deformed material through grain nucleation and growth by the stored energy of deformation (Doherty et al. 1997). The effect of recrystallization on 5083-H116 is shown in Figure 24. The elongated (textured) as-received grain structure (Figure 24a) recrystallizes to form equiaxed grains (Figure 24b). The average grain sizes are 89 and 48 μm in the as-received and recrystallized states, respectively. The grain size strengthening contributions before and after recrystallization were calculated to be 23 and 32 MPa using the Hall-Petch relationship ($\sigma_y = \sigma_0 + kd^{-1/2}$) with $k = 0.22$ MPa/m$^{1/2}$ (Last and Garrett 1996). The increased grain strengthening is counteracted by strength reduction due to subgrain annihilation from grain boundary migration during grain growth (Dieter 1976). The net result is a strength reduction of ~110 MPa following heat exposure (see Figure 20a). Huskins, et al. (2010) estimated subgrain boundary strengthening to be ~4.5 times greater than that of grains.

6061-T651 mechanical properties

6061-T651 undergoes a single stage of property reduction. All characteristics of residual mechanical behavior experience significant evolution, including yield strength (Figure 20b), ultimate strength (Figure 21), $d\sigma/d\varepsilon$ (Figure 19b), and ductility (Figure 22). Yield strength degradation initiates at 200°C and progressively decreases with increasing temperature. It also exhibits significant heating rate dependence. Precipitate growth and precipitate volume fraction reduction govern the residual mechanical behavior.

It is widely accepted that the primary strengthening phase in 6061 is the metastable β″ phase, which is shown in Figure 25. The interaction of this phase with dislocations governs strength. Growth of the strengthening phase at elevated temperatures weakens this interaction, thereby reducing yield strength. The sequence and morphology of 6061 precipitate growth has been the topic of numerous studies (Edwards et al. 1998; Gupta et al. 2001; Gaber et al. 2006). The generally accepted sequence is SSSS (supersaturated solid solution) → clusters/Guinier-Preston zones → β″ → β′ → β (Mg_2Si). The detailed evolution is given from DSC analysis of 6005A-T6 at 20°C/min (Simar et al. 2008):

- the β″dissolution peak is identified at ~260°C;

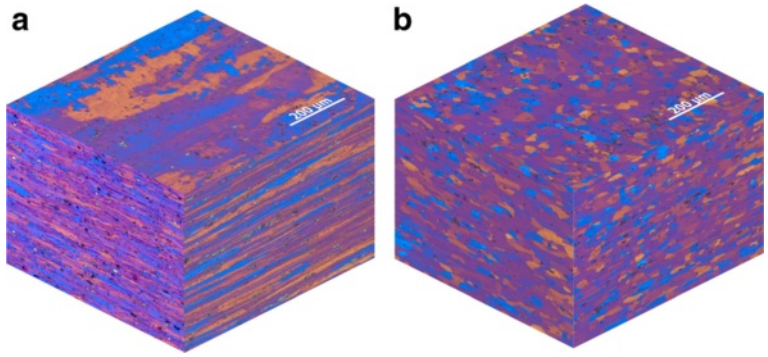

Figure 24 5083-H116 grain morphology **(a)** as-received and **(b)** recrystallized after 400°C exposure at 20°C/min.

- the β′ precipitation peak is identified at ~310°C;
- a broad β′ dissolution peak occurs from ~350 – 420°C;
- the β precipitation peak is identified at ~460°C;
- the β dissolution peak is identified at ~510°C.

β′ may also be formed directly by β″ coarsening rather than by dissolution and precipitation.

6061 yield strength reduction initiates at about 250 – 300°C (Figure 20b) which is also about when the hardening rate ($d\sigma/d\varepsilon$) begins to change (Figure 19b). These temperatures are associated with precipitate growth from the β″ to β′ phase (Simar et al. 2008). This is indicative of a transition in the governing strengthening mechanism, i.e., precipitate-dislocation interaction. This transition may be elucidated using the hardening rate and yield strength evolution. Below 250°C, $d\sigma/d\varepsilon$ remains low (<1000 MPa), as is associated with small precipitate dislocation shearing (Dieter 1976). The residual yield strength is also relatively unchanged from the as-received value. The strengthening mechanism transition is discernible after exposure to 300°C at 20°C/min, which reduces residual yield strength by 90 MPa. The hardening rate also increases to ~1600 MPa at the initiation of plastic flow. This indicates that both strengthening mechanisms are likely active in the alloy due to a precipitate size distribution (Simar et al. 2007). Further increasing temperature results in a significant increase in initial hardening rate (>3000 MPa). This is accompanied by a significant reduction in residual yield strength. This indicates large precipitates are a large proportion of the remaining precipitate distribution; the governing strengthening mechanism is thus predominantly Orowan looping (Dieter 1976).

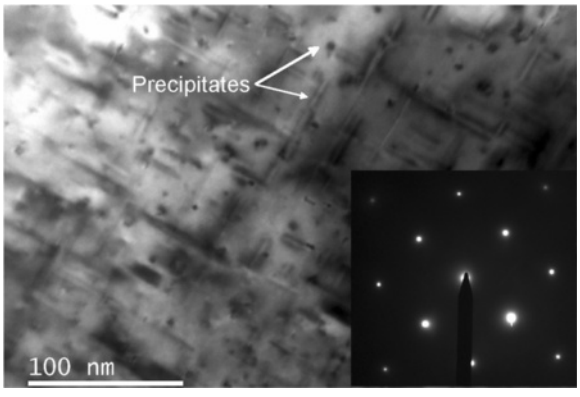

Figure 25 6061-T651 β″ precipitates in the as-received state imaged using bright-field TEM.

6061-T651 residual mechanical behavior time-temperature dependence is well-described using the kinetic-dependence of the strengthening phase. As noted previously, the strengthening precipitate/dislocation interaction is defined in terms of precipitate size and volume fraction. Therefore, the details of precipitate growth and evolution may elucidate the time-temperature dependence of the residual mechanical behavior. Doan, et al. (2000) examined 6061 strengthening phase precipitation using DSC at heating rates of 5 – 20°C/min. A heating rate increase from 5 to 20°C/min resulted in β″, β′, and β-phase precipitation peak temperature increases of 30, 35, and 43°C, respectively. Similarly, the β″-phase precipitation peak temperature in an Al-1.1wt%Mg_2Si alloy was measured to increase by 43°C for a heating rate increase from 5 to 50°C/min (Gaber et al. 2006). The measured 6061-T651 residual yield strength evolution (Figure 20b) is similar to that for precipitate evolution in Refs. (Gaber et al. 2006) and (Doan et al. 2000). The residual mechanical behavior observed in this work is also reasonably reflected by that of Maisonnette, et al. (2011) for 6061-T6, which was previously exposed at high heating rates, i.e., 30 – 12000°C/min.

Residual mechanical behavior – thermomechanical damage

Aluminum structures experience both thermal exposure and mechanical loading during a fire. The effect of mechanical loading, and its induced damage, is in contrast to the purely thermal considerations of the prior section. Mechanically-induced stress plays an important role accelerating damage development in load-bearing structures.

Damage manifests itself during elevated temperature exposure as large plastic (creep) deformation, grain elongation, dynamic dislocation recovery, precipitate cracking, and cavity formation (Leckie and Hayhurst 1974; Lin et al. 2005). These effects accumulate, developing a stress-induced damage state which may cause pre-mature failure of the structure.

In this section, the effect of thermomechanically-induced damage on residual mechanical behavior of 5083-H116 and 6061-T651 is presented. Materials subjected to prior damage both thermally (unstressed during prior elevated temperature exposure) and thermomechanically (stressed during prior elevated temperature exposure) were tested to separate stress-induced damage from thermal effects only. In thermomechanical tests, samples were heated at a constant heating rate (5083 – 50°C/min, 6061 – 20°C/min) to the desired temperature. Stress was then applied while the sample was held isothermally at this temperature, thus inducing creep deformation. These tests were stopped after defined durations to investigate damage at several creep strains. Stress-free thermal exposure tests were also performed at the same time-temperature conditions without stress. Thus, the effect of prior thermomechanical exposure on residual mechanical properties may be elucidated. Refer to Chen (2014) for details regarding specimen geometry, testing machine details, heating apparatus, and strain measurement.

Stress-induced damage in 5083-H116

As discussed previously, 5083-H116 thermally-induced strength degradation is attributed to two microstructural changes: (i) an initial strength reduction below about 280°C caused by subgrain coarsening during dislocation recovery and (ii) a significant strength reduction from about 280 – 380°C due to recrystallization. Thus, tests were performed at several temperatures in an effort to separate stress-induced damage from thermally-induced microstructural evolution: 200°C (subgrain coarsening and initial strength degradation), 300°C (initiation of recrystallization), and 400°C (fully recrystallized material). The following discussion references material planes and directions as depicted in Figure 26. All samples were loaded along the rolling direction.

Cavitation development

Thermomechanical exposure results in internal cavitation (void development) as a type of stress-induced damage. Cavity nucleation, growth, and coalescence are a primary cause of creep rupture. Cavity nucleation requires significant stress concentration orders of magnitude greater than the applied stress (Evans 1984; Kassner & Hayes 2003). Stress concentrations also aid cavity nuclei growth during its incipient stages, although initial growth is also aided by absorption of lattice vacancies (Greenwood et al. 1954).

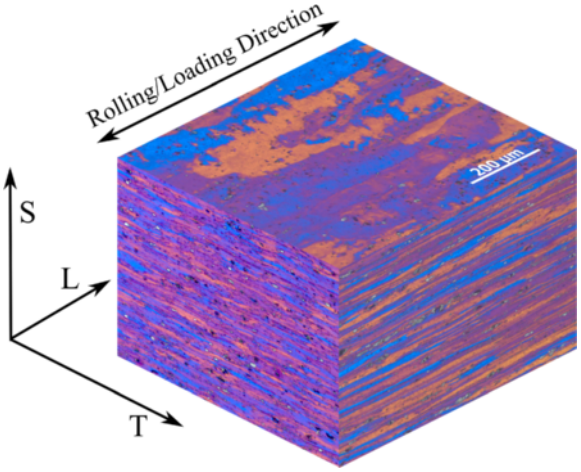

Figure 26 Material plane/direction definition related to 5083-H116 grain structure.

Grain boundary sliding and dislocation pile-up generate sufficient local stresses to promote cavity formation, particularly at precipitates located at grain boundaries (Yoo and Trinkaus 1986; Trinkaus and Yoo 1987). Existing cavities also cause stress concentrations resulting in new cavity formation with increasing creep strain (Anderson and Shewmon 2000). Once formed, cavity growth is primarily driven by two mechanisms: vacancy diffusion and creep plasticity (Hulla and Rimmera 1959; Hancock 1976; Raj and Ashby 1975). Comparison of diffusive cavity growth and plastic cavity growth has demonstrated cavities grow faster when driven by plasticity. Grain boundary sliding has also been considered a mechanism for cavity growth (Chen 1983).

Thermomechanical cavitation damage was induced by creep deformation (refer to Section 3.7 for 5083-H116 creep behavior). Cavitation development was quantified using scanning electron microscopy (SEM) and optical microscopy. Refer to Chen (2014) for further details including the quantitative microscopy methods used to determine cavity fraction.

Microstructures are compared for samples previously thermally and thermomechanically exposed at several temperatures and stress states in Figure 27. Note, all samples were exposed for the same duration – 2000 s. Figure 27a-c illustrates thermal exposure without applied stress. As expected, no cavitation is observed indicating that thermal exposure does not solely cause cavity formation. In contrast, cavities develop in thermomechanically damaged samples (Figure 27d-f) due to local stress concentrations. Following nucleation, cavity growth is governed by diffusion when small, then by diffusion and creep plasticity, and finally by creep plasticity alone (Cocks and Ashby 1982). Thus, cavity development is primarily dependent on the plastic strain. Thermomechanically damaged sample microstructures are

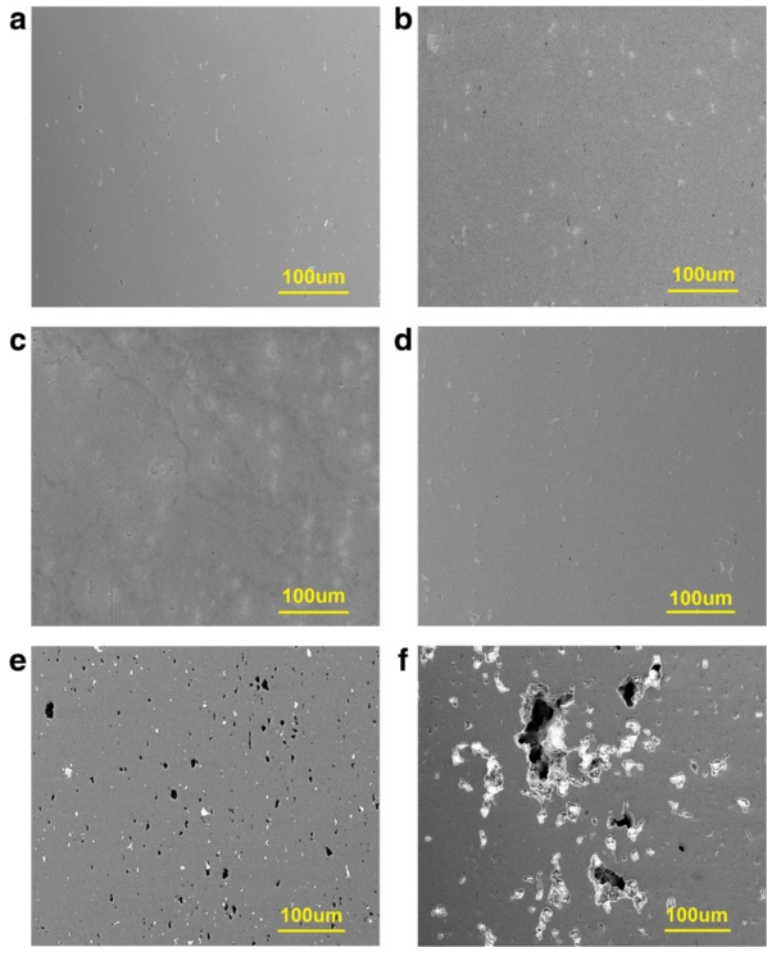

Figure 27 Comparison of **(a)-(c)** thermally and **(d)-(f)** thermomechanically damaged 5083-H116 samples exposed for 2000 s. The shown conditions are **(a)** 200°C, **(b)** 300°C, **(c)** 400°C, **(d)** 200°C, 140 MPa, ε = 15%, **(e)** 300°C, 50 MPa, ε = 100% and **(f)** 400°C, 17 MPa, ε = 143%. The rolling/loading direction for all micrographs is along the long axis of the page.

shown for the same exposure duration (2000 s) in Figure 27d-f. Cavity size and volume fraction are observed to increase with creep strain. The plasticity contribution to damage may be inferred from the material's high temperature ductility (see Figure 11) which increases with temperature (Allen 2012). At 200°C (Figure 27d), the exposure resulted in low plastic strains (15%) with minimal cavitation. Samples exposed to 300 and 400°C were plastically strained to 100 and 143%, respectively. Small spherical cavities appear at 300°C (100% plastic strain). At 400°C (143% plastic strain), large localized strains occur driving small cavities to coalesce into larger, irregular shaped cavities randomly distributed in the sample (Goods and Nix 1978).

Creep tests performed to induce thermomechanical damage at 400°C were interrupted at strains of 50 – 143% for 17 MPa; 100 – 133% for 15 MPa; and 100 – 144% for 14 MPa, as shown in Figure 28. The tests shown were used to investigate development of thermomechanical damage.

Cavitation evolution with increasing creep strain is shown in Figure 29 for creep conditions of 400°C and 17 MPa applied stress. The as-received material has no cavities (Figure 29a). At creep strains less than 100% (Figure 29b,c), cavities appear as randomly distributed small, spherical voids. As the creep strain surpasses 100% (Figure 29d), cavities begin to agglomerate into more irregular, slightly elongated voids. This indicates cavity coalescence initiates at creep strains between 80 and 100% (for this particular temperature and stress). As the material approaches failure (i.e., 143% creep strain in Figure 29e), the spherical cavities continue coalescing, forming highly elongated, crack-like cylindrical voids parallel to rolling/loading direction. Cavity lengths range from 50 – 150 μm with aspect ratios greater than five.

Thermomechanical creep damage was quantified using cavity volume fraction and cavity size. Cavity evolution after creep deformation at 400°C is shown in Figure 30. Note, the error bars signify the standard deviation of cavity

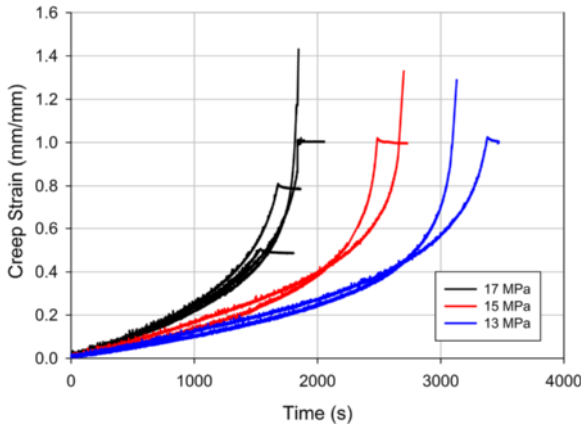

Figure 28 5083-H116 creep behavior at 400°C for several applied stress levels.

volume fraction calculated from 30 micrographs. At 17 MPa, cavity volume fraction gradually increases to 1% at strains less than 100%; however, continued creep deformation results in a significant increase in the rate of cavity growth. The critical cavity volume fraction before sample failure, i.e., 143% creep strain, is relatively small (~4.7% for 17 MPa). A similar trend was observed for applied stresses of 15 and 14 MPa.

Grain structure evolution

Thermomechanical deformation induces grain structure evolution, including changes in size, shape, and texture. Dynamic recrystallization also occurs during high temperature, high strain creep deformation. Grains elongate with increasing strain prior to the onset of dynamic recrystallization. The effect of grain elongation on strength has been studied (Bunge et al. 1985) including development of a model coupling grain orientation and grain size/shape (Sun and Sundararaghavan 2012). Yield strength increases as the structure elongates

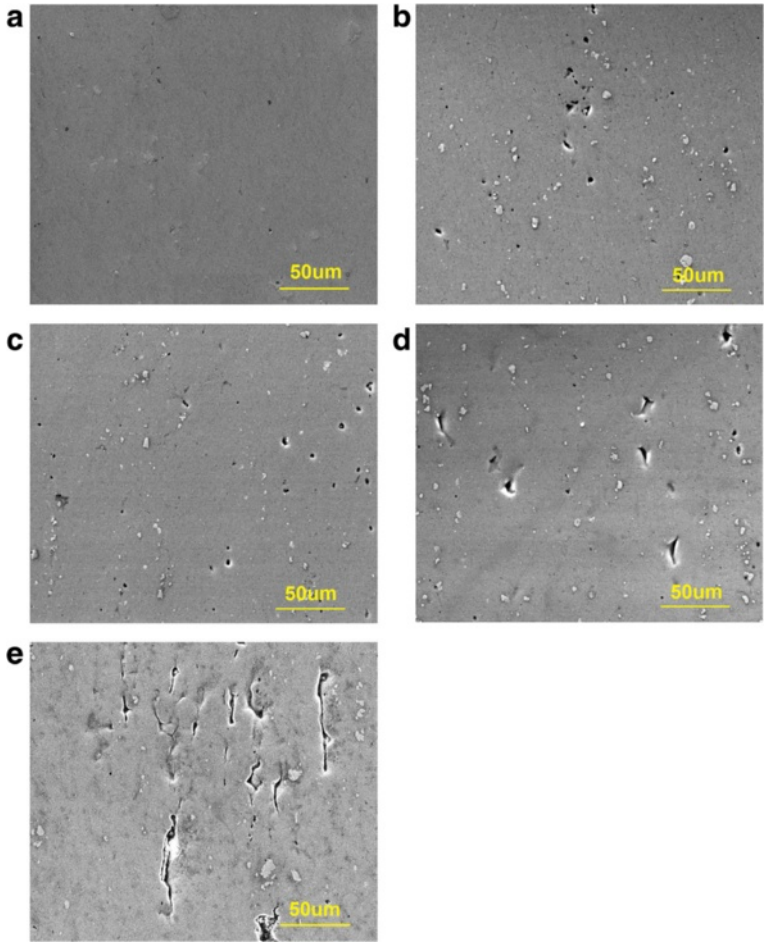

Figure 29 SEM micrographs of thermomechanically (creep) damaged 5083-H116 at 400°C including **(a)** thermal exposure only, and 17 MPa applied stress strained to **(b)** ε = 50%, **(c)** ε = 80%, **(d)** ε =100%, and **(e)** ε = 143%. The rolling/loading direction is along the long axis of the page.

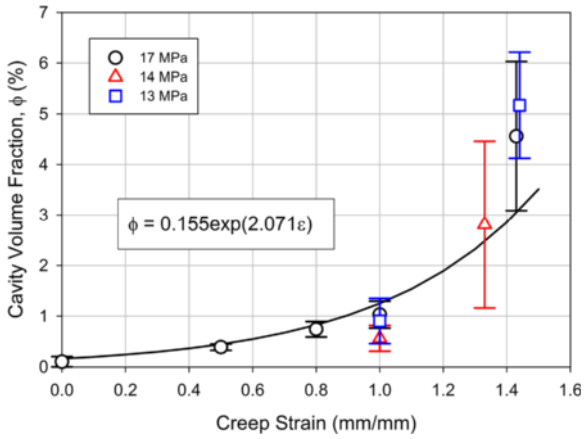

Figure 30 Cavity volume fraction as a function of creep strain at 400°C. An exponential fit between cavity volume fraction and creep strain is also shown.

from a recrystallized (equiaxed) grain structure to an elongated one with high aspect ratio grains (Liu et al. 2014).

Almost no grain structure evolution was observed after thermal exposure at 200°C. This is expected based on previous discussion in the 5083-H116 mechanical properties section. The thermomechanically strained samples have a grain structure similar to that in the as-received state with minimal evolution in terms of size and shape.

The grain structure evolution after prior thermal exposure at 300°C (50°C/min heating rate) with various isothermal holds is shown in Figure 31. As discussed previously, grain recrystallization initiates between about 280 – 320°C depending on heating rate. The grain structure upon reaching 300°C after heating at 50°C/min (Figure 31b) is not significantly recrystallized. Isothermal holds at 300°C (after 50°C/min heating) result in recrystallization, which initiates as nuclei at areas of high stored strain energy (e.g., intermetallic precipitates and grain boundaries) followed by grain growth (Summers 2014; Vandermeer and Juul Jensen 2001). A partially recrystallized grain structure is shown in Figure 31c after isothermal exposure at 300°C for 500 s. Further isothermal exposure for 1000 s (Figure 31d) results in a nearly fully recrystallized grain structure.

Thermomechanically strained samples exhibit a different morphological evolution during recrystallization as compared to those only thermally exposed, as shown in Figure 32 for 300°C, 50 MPa. As strain increases with increasing exposure time, the grain structure elongates in the loading direction; however, this is not overtly obvious at lower creep strains. Samples with 13 – 30% creep strain (Figure 32a-c) have slightly elongated and narrowed grains compared to the as-received state (Figure 31a). At 100% creep strain (Figure 32d), the grains are highly elongated and significantly narrowed; the grain aspect ratio is significantly higher than as-received, as shown in Figure 33. The as-received grain aspect ratio (~3.2) increases to ~8.2 at 77% reduction of area. The grain boundaries also become serrated; some pinch off to form new grains. This phenomenon is known as geometric dynamic recrystallization (GDRX). GDRX occurs during severe plastic deformation as grains increasingly flatten until the boundaries on all sides are separated by a relatively small distance, thus the serrated boundaries will come into contact to form new grains (Konopleva et al. 1995).

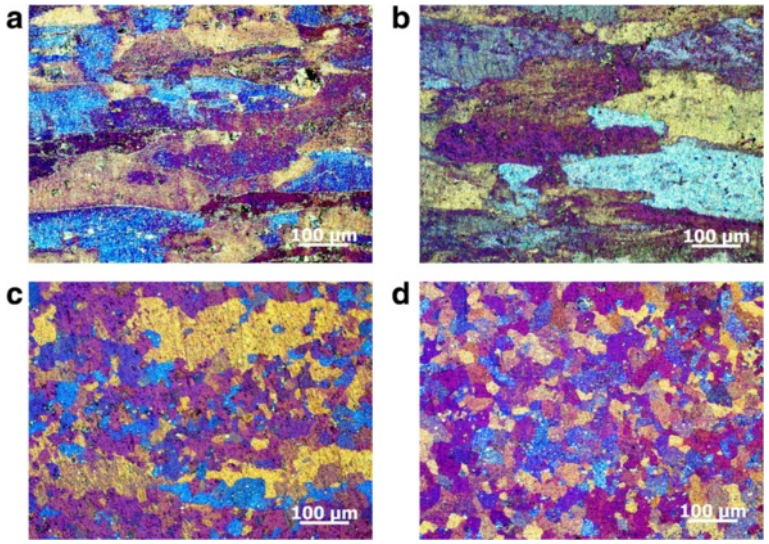

Figure 31 5083-H116 grain structure (LT surface) in the **(a)** as-received state, and after prior thermal exposure (no applied stress) at 300°C for **(b)** 0 s, **(c)** 500 s, and **(d)** 1000 s.

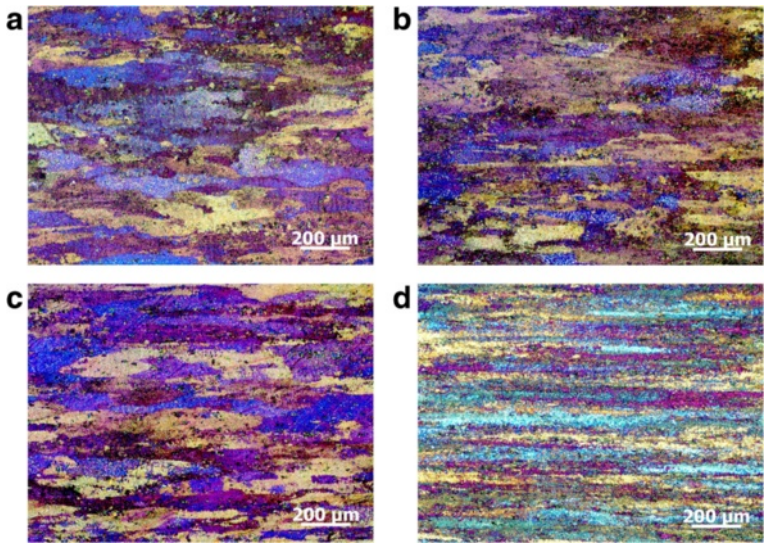

Figure 32 5083-H116 grian structure (LT surface) after prior thermomechanical creep deformation at 300°C, 50 MPa to **(a)** 500 s, ε = 13%, **(b)** 1000 s, ε = 20%, **(c)** 1500 s, ε = 30%, and **(d)** 2000 s, ε = 100%.

Residual mechanical behavior

The residual mechanical behavior is also affected by prior thermomechanical exposure; it is governed by the previously described dynamical microstructural evolution, i.e., dynamic dislocation recovery, grain elongation, and GDRX. Residual yield and ultimate strength is shown as a function of creep strain during prior thermal-only and thermomechanical exposure in Figure 34.

In Figure 34, samples heated to 300°C at 50°C/min (followed by immediate water quenching, no applied stress) exhibit a slight reduction in yield strength (~60 MPa) and ultimate strength (~30 MPa) caused by static dislocation recovery and partial recrystallization. Additional isothermal exposure at 300°C results in continued recrystallization until an equilibrium is reached at about 1000 s (Figure 31).

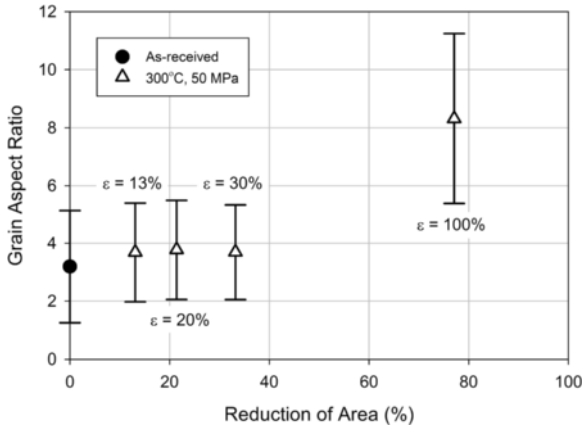

Figure 33 5083-H116 grain aspect ratio (calculated based on rolling surface grains) resulting from interrupted thermomechanical creep tests at 300°C and 50 MPa.

No further strength reduction occurs as evidenced by a nearly constant yield strength (~150 MPa).

The effect of thermomechanical creep damage on the residual mechanical behavior is also shown in Figure 34. Note, residual mechanical properties of strained samples are calculated based upon the deformed (post-creep) cross-sectional area – an effective true stress calculation. Prior creep strains of 13 – 30% result in a small strengthening effect; the effect becomes significant at higher strains. After prior deformation to 100% creep strain, yield and ultimate strength increase by ~120 MPa and ~50 MPa, respectively. This is primarily attributed to grain elongation and GDRX. Research suggests the increase in strength is related to the grain aspect ratio, which is indicative of the potential formation of a dislocation cell (subgrain) structure, especially at high aspect ratios (Sun and Sundararaghavan 2012). Grain thickness is also significantly reduced (Liu et al. 2014). These mechanisms are similar to hot rolling which is a common material processing technique. Cavities nucleate, grow, and coalesce simultaneously with grain morphology evolution in the highly strained sample (see the micrographs in Figure 34b and c). As such, a competing process exists where grain elongation strengthens the material and cavities effectively weaken it by reducing the cross-sectional area. At 100% creep strain, the cavity volume fraction is relatively low (~1.5%), thus, it may be concluded that grain elongation governs residual strength in this case.

Stress-induced damage in 6061-T651

As discussed previously, 6061-T651 thermally-induced strength degradation is attributed to coarsening and dissolution of the strengthening β″ phase. This significantly affects the precipitate-dislocation interaction which effectively

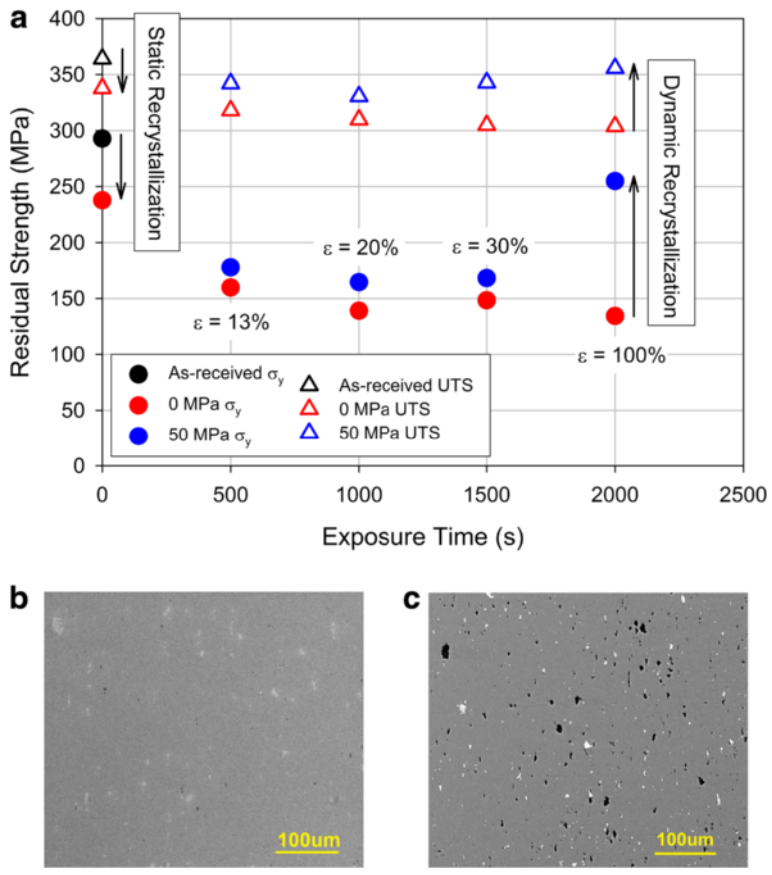

Figure 34 5083-H116 residual mechanical behavior **(a)** after thermal exposure at 300°C and thermomechanical creep damage at 300°C, 50 MPa along with pictures of the cavitation present at **(b)** 30% and **(c)** 100% creep strain.

governs the alloy's yield strength (Summers et al. 2014). The minimum yield strength is reached when the strengthening phase has significantly coarsened and dissolved while not reverting to a supersaturated solid solution, which occurs at about 400°C when heated at 20°C/min. Thus, thermomechanical tests were performed at 400°C in an effort to separate stress-induced damage from thermally-induced microstructural evolution.

Cavitation development

Thermomechanical cavitation damage was characterized similar to 5083-H116 (refer to Section 3.7 for 6061-T651 creep behavior). Microstructures are compared in Figure 35 for samples previously thermally and thermomechanically exposed at 400°C and up to 20 MPa. As expected, thermally exposed samples have no cavities (Figure 35a-c). A large number of cavities are visible after creep deformation to 58% strain (Figure 35d). This strain level is just before fracture thus signifying the maximum amount of cavitation damage expected at this particular temperature and stress. The cavities are small, spherical voids (Figure 35d) at creep rupture as compared to the elongated, cylindrical cavities in 5083 (see Figure 28f and Figure 29e). Note, 6061 cavitation evolution at 300°C is similar to that observed at 400°C.

Grain structure evolution

Grain structure evolution after prior thermal and thermomechanical exposure at 400°C is shown in Figure 36. The as-received grain structure (Figure 36a) is mostly equiaxed with a slight elongation in the rolling direction. The grain structure does not change significantly due to thermal exposure only (Figure 36b). Note, the large grain size in 6061 contributes insignificantly to its strength (Summers 2014). The thermomechanically exposed samples (20 MPa applied stress) have been creep deformed to relatively high levels (refer to Figure 17); 6061 accumulates about 60% creep strain with about 75% reduction of area before creep rupture. In Figure 36c-f, grains are observed to elongate along the rolling/loading direction. Grain aspect ratio increases with reduction in area, as detailed in Figure 37. The as-received grain aspect ratio (~1.3) increases to ~2.2 at 33% reduction of area. Grain aspect ratio significantly increases to 6.35 just before creep rupture; however, unlike for 5083, insufficient plastic deformation has occurred to cause GDRX.

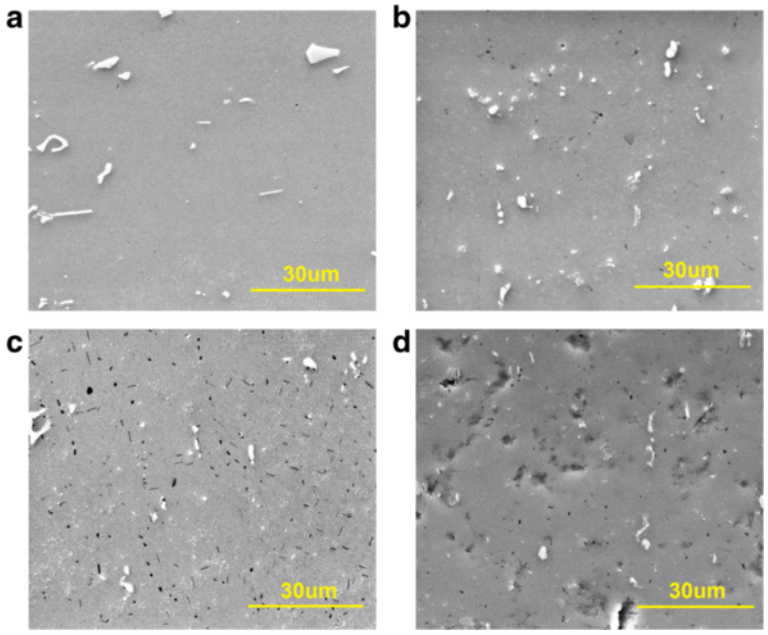

Figure 35 Comparison of **(a)-(c)** thermally and **(d)** thermomechanically damaged 6061-T651 samples. The conditions shown are for **(a)** as-received, and at 400°C for **(b)** 0 s, **(c)** 2900 s, and **(d)** 2900 s at an applied stress of 20 MPa resulting in $\varepsilon = 58\%$.

Residual mechanical behavior

6061-T651 residual mechanical behavior after prior thermomechanical exposure is governed by the normal static process, i.e., precipitate growth and dissolution, and by dynamic processes including dynamic precipitation and grain elongation. Grain elongation has only a minor effect on strength as the reduction in area is significantly less than for 5083.

In Figure 38, samples heated to 400°C at 20°C/min (no applied stress) were measured to have a relatively constant residual strength after 1000 s of isothermal exposure. The effect of thermomechanical creep damage at 400°C, 20 MPa on residual mechanical behavior is also shown in Figure 38. Note, residual mechanical properties of strain samples are calculated based upon the deformed (post-creep) cross-sectional area – an effective true stress calculation. A negligible strengthening effect is measured at low creep strains as both cavitation (weakening) and grain elongation (strengthening) are minimal at small strain levels. A yield strength increase of ~40 MPa was measured after prior creep deformation to higher strains, i.e., $\varepsilon \geq 43\%$. This is primarily caused by grain elongation with negligible cavitation. All cavities remain small and spherical until failure; the cavity volume fraction before creep failure at 400°C is only 1.9%. In contrast, grain aspect ratio significantly increases to ~6.4 just before rupture.

Residual mechanical behavior prediction

Several models have been developed to predict the residual mechanical constitutive behavior of 5083-H116 and 6061-T651 following a fire exposure. These models include simplistic empirical yield strength models and physically-based constitutive models for residual yield strength.

Empirical models

Summers, et al. (2014) developed empirical models to estimate the residual yield strength of 5083-H116 and 6061-T651 after a fire. Conservative estimates of the residual yield strength after infinite isothermal exposure, i.e., infinite time at a given temperature, are shown in Figure 39 (5083-H116) and Figure 40 (6061-T651). The conservative estimates were determined using the residual yield strength models in Ref. (Summers 2014). The time-temperature dependence of residual yield strength should be considered for shorter duration exposures. Material heating during a fire may be idealized as linear (ramp) heating followed by isothermal heating. Aluminum alloy structural members have been measured to approximate such a heating profile during standard fire resistance tests (Suzuki et al. 2005).

Thus, empirical models have been developed to estimate residual yield strength after linear heating (experimental data in Ref. (Summers 2014)) and isothermal heating (models in Ref. (Summers 2014)). The linear heating empirical models are valid within the bounds of the heating rates tested, i.e., 5 – 250°C/min. Lower heating rates may be conservatively approximated using the isothermal heating empirical models.

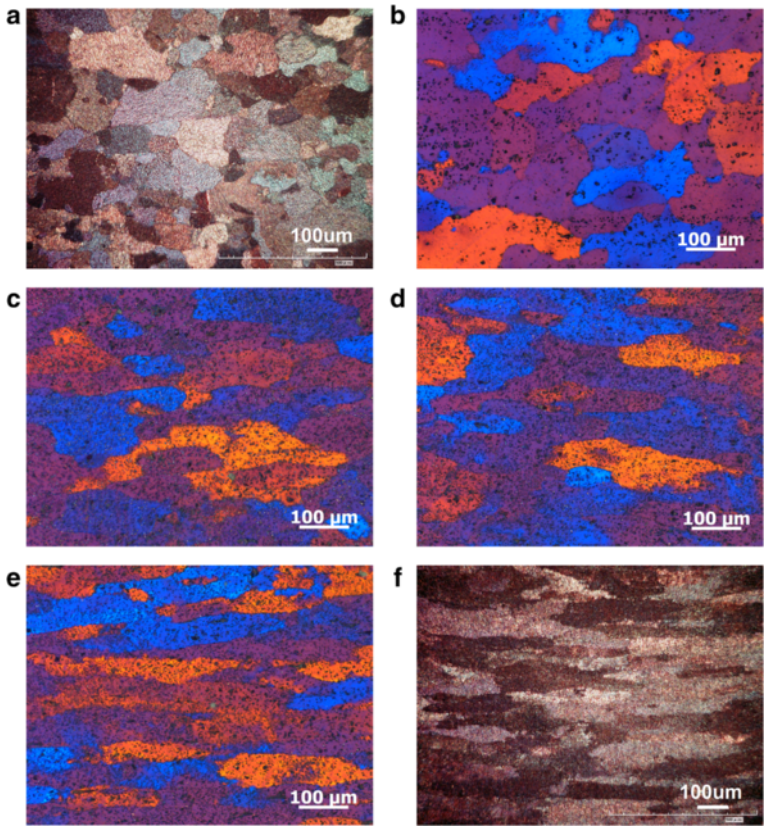

Figure 36 6061-T651 grain structure (LT surface) in the **(a)** as-received state, **(b)** thermally exposed at 400°C for 0 s, and thermomechanically strained at 400°C, 20 MPa to **(c)** ε = 25%, **(d)** 36%, **(e)** 47%, and **(f)** 58%. Rolling/loading direction is across the width of the page.

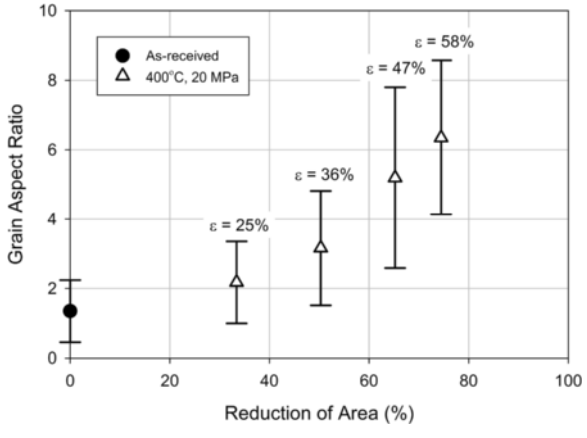

Figure 37 6061-T651 grain aspect ratio (calculated based on rolling surface grains) resulting from interrupted thermomechanical creep tests at 400°C and 20 MPa.

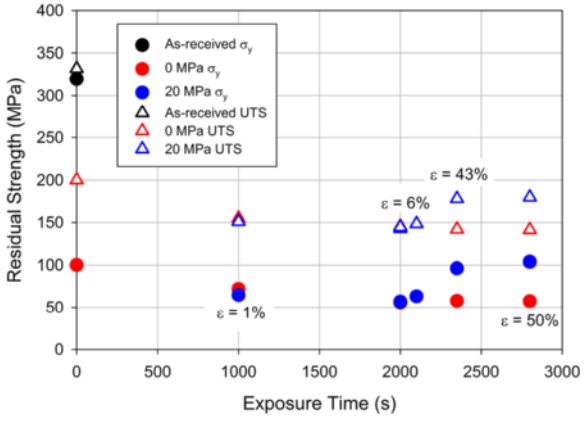

Figure 38 6061-T651 residual mechanical behavior after thermal exposure at 400°C (0 MPa) and thermomechanical creep damage at 400°C, 20 MPa.

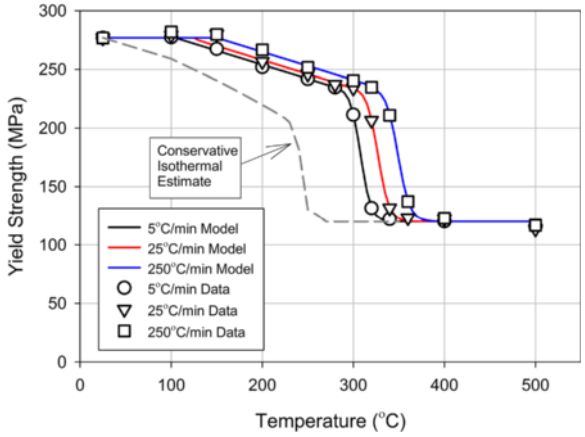

Figure 39 Comparison of 5083-H116 residual yield strength predicted using the model described through Eqns. (13) – (15) and experimental data after heating at 5, 25, and 250°C/min.

5083-H116

5083-H116 residual yield strength was estimated for linear heating using the following relations:

$$T_c \leq 100°C \qquad \sigma_y = \sigma_{y,AR} \tag{13}$$

$$100°C < T_c \leq 280°C \qquad \sigma_y = (-0.24)\ T_c + a \tag{14}$$

$$T_c > 280°C \qquad \sigma_y = \frac{\sigma_{y,AR} + \sigma_{y,RX}}{2} - \frac{\sigma_{y,AR} - \sigma_{y,RX}}{2} \tanh[\phi(T_c - T_k)] \tag{15}$$

where T_c is the final exposure temperature (°C), σ_y is the estimated residual yield strength (MPa), and a (MPa), ϕ (-), and T_k (°C) are heating rate dependent parameters.

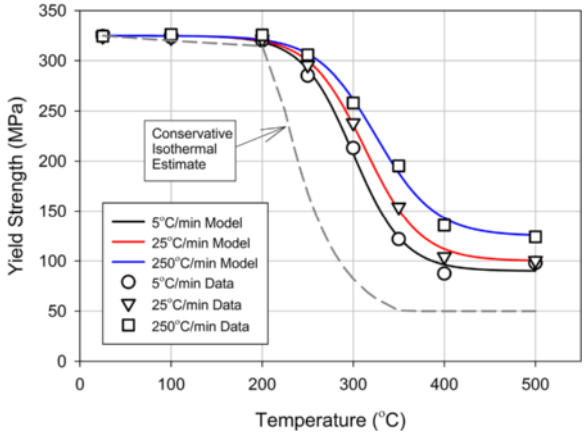

Figure 40 Comparison of 6061-T651 residual yield strength estimated using Eq. (19) and experimental data after heating at 5, 25, and 250°C/min.

The as-received ($\sigma_{y,AR}$ = 277 MPa) and recrystallized ($\sigma_{y,RX}$ = 120 MPa) yield strengths are taken as that from experiment (Figure 20a). The remaining parameters, given in Table 5, were determined by non-linear least squares regression for each heating rate. The empirical evolution models in Eqs. (13) – (15) are compared against experimental data in Figure 39 with good agreement. Note, the effect of heating rates between 5°C/min and 250°C/min may be estimated using interpolation.

The isothermal exposure empirical models were developed using the 5083-H116 residual yield strength model from Ref. (Summers 2014). The isothermal behavior is separated into two regions dependent on whether the material initiates recrystallization within 10 hours of exposure. This was determined to be 230°C. The relations are as follows

$$T_c \leq 230°C \qquad \sigma_y = \sigma_{y,AR}(bt)^c \tag{16}$$

$$T_c > 230°C \qquad \sigma_y = (\sigma_{y,AR} - \sigma_{y,RX}) \exp[dt] + \sigma_{y,RX} \tag{17}$$

where t is time (s) and b (1/s), c (-), and d (1/s) are temperature-dependent parameters defined as

$$parameter = \alpha \exp(\beta T_{iso}) \tag{18}$$

where T_{iso} is the isothermal exposure temperature (°C) and α (units dependent on parameter) and β (1/°C) are fitting parameters, which are given in Table 6 for parameters in Eqs. (16) and (17).

6061-T651

6061-T651 residual yield strength was estimated for linear heating using the following relation

$$\sigma_y = \frac{\sigma_{y,AR} + \sigma_{y,min}}{2} - \frac{\sigma_{y,AR} - \sigma_{y,min}}{2} \tanh[\phi(T_c - T_k)] \tag{19}$$

where $\sigma_{y,min}$ (MPa), ϕ, and T_k are heating rate dependent parameters. The as-received yield strength ($\sigma_{y,AR}$ = 325 MPa) is that from experiment (Figure 20b). The remaining parameters, given in Table 7, were determined by non-linear least squares regression for each heating rate. The empirical evolution model in Eq. (19) is compared against experimental data in Figure 40 with good

Table 5 Parameters for the 5083-H116 linear heating empirical model in Eqs. (13) – (15)

	5°C/min	25°C/min	250°C/min
a (MPa)	302	306	313
φ (1/°C)	0.088	0.082	0.077
T_k (°C)	308	327	349

Table 6 5083-H116 isothermal empirical model parameter constants for use in Eq. (18)

Parameter	α	β (1/°C)
b (1/s)	0.0014 1/s	0.0166
c	-0.01	0.006
d (1/s)	-3.2 x 10^{-11} 1/s	0.062

agreement. As with 5083-H116, interpolation may be used to estimate heating rates between the relation bounds.

The empirical isothermal exposure model was developed using the residual yield strength evolution model from Ref. (Summers 2014). The relation is as follows

$$\sigma_y = \left(\sigma_{y,AR} - e\right) \exp[ft] + e \tag{20}$$

where e (MPa) and f (1/s) are temperature-dependent functions defined using Eq. (18). α and β in Eq. (18) are given for 6061-T651 in Table 8.

Kinetics-based predictions – strain hardened aluminum alloys

A physically-based constitutive model for strain hardened aluminum alloys based on kinetically (time-temperature) dependent microstructural evolution is detailed, including models for residual yield strength and strain hardening behavior. This model was previously implemented by (Summers 2014) for 5083-H116.

The physically-based constitutive models utilize microstructural evolution models to predict the residual mechanical state after elevated temperature exposure. The governing microstructural processes in 5xxx-series aluminum alloys are recovery and recrystallization (Dieter 1976). Reduction in the α-matrix Mg solute concentration also affects residual strength; however, this occurs at much longer time scales than expected in a fire scenario (refer to Ref. (Summers et al. 2014) for further discussion). Recovery is the process by which a previously deformed material lowers its internal energy state at low annealing temperatures (Dieter 1976), resulting in dislocation structure (dislocation cells/subgrains) coarsening (Xing et al. 2006; Furu et al. 1995; Hasegawa and Kocks 1979; Verdier et al. 1998b). In the static case, recovery proceeds as a thermally activated, kinetic process (Furu et al. 1995). Recrystallization is the primary process by which the stored energy of deformation (from material processing) is released in strain hardened aluminum alloys (Doherty et al. 1997). The recrystallization process, including grain nucleation, migration, growth, and impingement, has been studied extensively (Bay and Hansen 1979; Bay and Hansen 1984; Fujita and Tabata 1973; Huang and Humphreys 1999; McQueen and Ryum 1985; Vandermeer and Rath 1990; Jones et al. 1979; Huang and Humphreys 2012), including development of predictive models, e.g., the classical uniform impingement KJMA model (Kolmogorov 1937; Johnson and Mehl 1939; AIME 135:416 and Avrami 1939), and physically representative models, e.g., the linear/uniform impingement microstructural path model of Vandermeer and Juul Jensen (Vandermeer and Juul Jensen 2001; Vandermeer and Juul Jensen 1994). Refer to Summers (Summers 2014) for further details regarding the background and theoretical underpinnings of the various models presented in the subsequent sections.

Table 7 Parameters for the 6061-T651 linear heating empirical model in Eq. (19)

	5°C/min	25°C/min	250°C/min
$\sigma_{y,min}$ (MPa)	90	100	125
φ (1/°C)	0.0179	0.0165	0.0154
T_k (°C)	300	313	325

Table 8 6061-T651 isothermal empirical model parameter constants for use in Eq. (18)

Parameter	α	β (1/°C)
e (MPa)	2000 MPa	-0.01
f (1/s)	2.48 x 10^{-8} 1/s	0.0345

Residual yield strength model

A microstructure-based residual yield strength model was also developed for 5083-H116. Non-isothermal recovery and recrystallization models were implemented to predict microstructural evolution, and its effect on strength, after prior thermal exposure. The models were developed considering non-isothermal thermal exposures, which approximate the initial transient heating during a fire (see Summers (2014)).

Aluminum alloy as-received and residual yield strength is governed by the relative state and magnitude of the microstructural strengthening contributions. For 5083-H116, this includes (i) the friction stress (σ_0), (ii) the solid solution content (σ_{ss}), (iii) precipitate contributions (σ_p), (iv) grain contributions ($\Delta\sigma_g$), and (v) subgrain contributions ($\Delta\sigma_{sg}$). These are linearly superposed to calculate the total yield strength (σ_y) as

$$\sigma_y = \sigma_0 + \sigma_{ss} + \sigma_p + \Delta\sigma_{sg} + \Delta\sigma_g \tag{21}$$

Linear superposition is assumed valid as the individual microstructural features strengthen at different length scales, thus there is negligible interaction. The solid solution strengthening contribution, σ_{ss}, is assumed constant due to the short duration exposures expected during fire (Summers et al. 2014). Precipitate strengthening, σ_p, is considered negligible due to a low concentration of intermetallic precipitates as observed during TEM analysis (Summers 2014). The subgrain strengthening contribution, $\Delta\sigma_{sg}$, is reduced by recovery and is annihilated during recrystallization; therefore,

recovery and recrystallization models were implemented to predict $\Delta\sigma_{sg}$ evolution after prior thermal exposure. The grain strengthening contribution, $\Delta\sigma_g$, is solely dependent on recrystallization.

The non-isothermal residual yield strength model is given as

$$\sigma_y = \sigma_{pure} + H\left(C_{Mg}\right)^n + \left[X_{RX}^{3/4} k_g d_{AR}^{-1/2} + (1-X_{RX}) k_g d_{AR}^{-1/2}\right] + (1-X_{RX}) G\sqrt{b\theta_m}\left(\frac{\delta_{AR}}{X_{RV}^2}\right)^{-1/2} \quad (22)$$

The first parameter on the right hand side includes the friction stress and effects of other minor hardening solutes (i.e., Fe and Si). The second parameter is from the solid solution strengthening model. The bracketed parameter group implements grain strengthening with the first and second terms representing grain nucleation and growth, and grain annihilation; respectively. Both processes are a function of the recrystallized fraction, X_{RX}. The fifth term on the right hand side implements subgrain strengthening, including subgrain coarsening as a function of the fraction recovered, X_{RV}, and subgrain annihilation, due to recrystallization, as a function of X_{RX}.

The residual yield strength is predicted using Eq. (22) with the fraction recovered, X_{RV}, and fraction recrystallized, X_{RX}, predicted by non-isothermal recovery and recrystallization models. Refer to Summers et al. (2014) and Summers (2014) for model details. Comparison with experimental data is shown in Figure 41. Model parameters are given in Table 9.

The experimentally measured residual yield strength after thermal exposure, including its time-temperature (heating rate) dependence, is well represented by the residual yield strength model predictions in Figure 41. The initial yield strength reduction is well predicted by the model, specifically recovery and subgrain strengthening models. The onset of recrystallization is also captured by the model. The yield strength evolution during recrystallization is predicted by the grain and subgrain strengthening models; the kinetics are predicted by the recrystallization model. The predicted yield strength after recrystallization has completed (126 MPa) is also in agreement with experimental data, with predicted contributions of $\sigma_{pure} = 19$ MPa, $\sigma_{ss} = 75$ MPa, $\Delta\sigma_{sg} = 0$ MPa, and $\Delta\sigma_g = 32$ MPa.

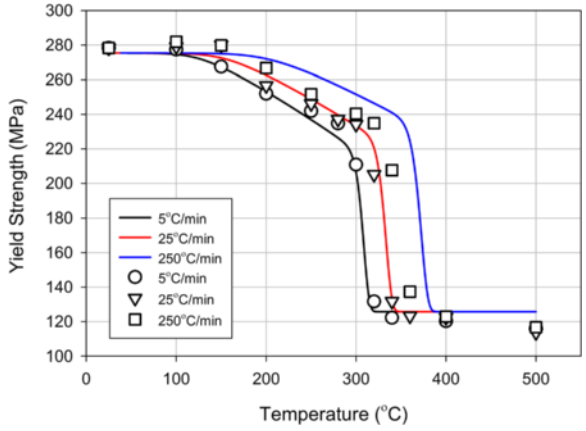

Figure 41 5083-H116 residual yield strength model predictions (lines) compared against experimental data (symbols).

Residual strain hardening model

Aluminum alloy strain hardening has been supposed to be the competitive evolution of the dislocation structure in terms of dislocation storage and dynamic recovery (dislocation annihilation or rearrangement) (Mecking and Kocks 1981; Estrin and Mecking 1984; Kocks 1976). Verdier and colleagues (Verdier et al. 1998a, b) considered the effects of a cellular dislocation structure (i.e., subgrains in 5083-H116) on strain hardening, including dislocation structure evolution during recovery. Recovery is shown to negligibly affect hardening rate except at stresses near yield (refer to Figure 19a). Recrystallization causes a significant hardening rate reduction at constant stress. The subgrains in 5083-H116 sequentially evolve during recovery (subgrain growth) and recrystallization (subgrain annihilation). Thus, subgrain annihilation is the mechanism which causes the hardening rate reduction during recrystallization. The KME model modified by Verdier et al. (1998a) was thus further adapted by Summers (2014) to include the effects of subgrain annihilation on 5083-H116 plastic deformation. Non-isothermal

Table 9 5083-H116 residual yield strength model parameters

Parameter	Significance	Value	Source
σ_{pure}	Friction stress including Fe, Si solutes	19.3 MPa	1050 (Ryen et al. 2006)
H	Constant for effect of Mg solutes on σ_{ss}	13.8 MPa/(Mg wt%)^n	(Ryen et al. 2006)
n	Hardening exponent for Mg solutes	1.14	(Ryen et al. 2006)
k_g	Hall-Petch constant for grain strengthening	0.22 MPa-m$^{1/2}$	(Last and Garrett 1996)
d_{AR}	As-received grain size	89 μm	(Summers et al. 2014)
d_{RX}	Recrystallized grain size	48 μm	(Summers et al. 2014)
G	Shear modulus	26400 MPa	
b	Magnitude of Burger's vector	0.286 nm	
θ_m	Mean misorientation angle of subgrains	2.7°	(Xing et al. 2006)
δ_{AR}	As-received subgrain size	376 nm	(Summers et al. 2014)

recovery and recrystallization models were implemented to predict subgrain and grain evolution.

The modified KME constitutive law (Verdier et al. 1998a) is defined as

$$\frac{d\sigma}{d\varepsilon} = \theta_0 + \frac{P_1}{\sigma} - P_2\sigma \tag{23}$$

where P_1 (MPa^2) represents subgrain dislocation storage and P_2 (-) is total dynamic recovery. P_1 and P_2 were modified by Summers (2014) as

$$P_1 = (1-X_{RX})M^3(\alpha G)^2\frac{b}{2\delta} \text{ and } P_2 = \frac{\theta_0}{\sigma_{sat,0}} + (1-X_{RX})\frac{K_{sg}M}{2\delta} \tag{24}$$

where δ is the predicted instantaneous subgrain size (nm) from the non-isothermal recovery model and $\sigma_{sat,0}$ is the theoretical saturation stress reached at infinite strain ($\sigma_{sat,0} = M\alpha Gb/L_0$). After recrystallization completes, i.e., $X_{RX} = 1$, the modified KME constitutive law reduces to the classical KME law, which does not account for dislocation structure effects.

Strain hardening is predicted using Eq. (24) with the predicted fraction recovered, X_{RV}, and fraction recrystallized, X_{RX}, predicted by non-isothermal recovery and recrystallization models. Refer to Summers (2014) for model details. All parameters of the modified KME model are provided in Table 10.

The modified KME model predictions are compared with experimental data (5, 25, and 250°C/min to 320°C) in Figure 42. The temperature chosen (320°C) spans a range of possible material states: fully recrystallized (5°C/min), partially recrystallized (25°C/min), and partially recovered (250°C/min). It is evident the model is capable of predicting strain hardening behavior after prior thermal exposure. The agreement between predictions and experiment is good at the shown conditions, which encompass those possible in 5083-H116. The strain hardening behavior approaches approximately the same saturation stress for all conditions as is expected from experiment.

Kinetics-based predictions – precipitation hardened aluminum alloys

A physically-based constitutive model for precipitation hardened aluminum alloys based on kinetically (time-temperature) dependent microstructural evolution is detailed, including models for residual yield strength and strain hardening behavior. This model was previously implemented by Summers (2014) for 6061-T651.

Numerous models are available in the literature for precipitate evolution, including analytical, internal variable models (Grong and Shercliff 2002; Myhr and Grong 1991a; Myhr and Grong 1991b; Bratland et al. 1997) and numerical class size models (Simar et al. 2007; Gallais et al. 2008; Esmaeili and Lloyd 2005; Deschamps et al. 1999; Myhr and Grong 2000; Myhr et al. 2001; Myhr et al. 2002; Nicolas and Deschamps 2003; Myhr et al. 2004; Khan et al. 2008; Perez et al. 2008; Bardel et al. 2014; Bahrami et al. 2012). The analytical approach fails when complicated diffusion processes are involved due to the interaction of different size precipitates (Grong and Shercliff 2002). This is the case for commercial alloys, e.g., 6061, in an aged (hardened) state, e.g., T4 or T6. A numerical class size model, which implements the complete precipitate size distribution (PSD), is therefore required. PSD evolution at elevated temperatures is commonly modeled using the Kampmann-Wagner numerical (KWN) model (Kampmann and Wagner 1984) is commonly implemented (Simar et al. 2007; Gallais et al. 2008; Esmaeili and Lloyd 2005; Deschamps et al. 1999; Myhr and Grong 2000; Myhr et al. 2001; Myhr et al. 2002; Nicolas and Deschamps 2003; Myhr et al. 2004; Khan et al. 2008; Perez et al. 2008; Bardel et al. 2014; Bahrami et al. 2012) in a finite difference formulation (Myhr and Grong 2000). The KWN model describes the nucleation, growth, and dissolution processes using a diffusion-based methodology assuming spherical precipitates.

The KWN model is an example of the so-called classical nucleation and growth theories (CNGTs) which have been widely implemented for modeling PSD evolution, including growth, nucleation, and dissolution. Myhr et al. (2001) and Deschamps and Bréchet (1998) initially adapted the KWN model to Al alloys by implementing a unique β″/β′ phase, thereby simplifying the complex precipitation sequence. This approach was extended to non-isothermal heat treatments in further work by (Myhr et al. 2004). These initial models have been extensively implemented for Al alloys (Simar et al. 2007; Gallais et al. 2008; Myhr et al. 2002; Myhr et al. 2004; Perez et al. 2008; Bardel et al. 2014; Bahrami et al. 2012) including adaptations for heterogeneous precipitation (Gallais et al. 2008; Myhr et al. 2002), various metastable precipitates (Myhr et al. 2002), ternary/quaternary phases (Gallais et al. 2008), and non-spherical precipitates (Bardel et al. 2014; Bahrami et al. 2012). (Perez et al. 2008) discussed the necessity of modeling PSD evolution using a class size approach rather than a mean radius approximation.

An integrated modeling approach was implemented by Summers (2014) to predict 6061-T651 residual yield strength and strain hardening as a function of PSD evolution. The KWN model implemented by Simar et al. (2007) provides a balance between representative capability and limited complexity. In this model, nucleation, growth, and dissolution processes are assumed to occur

Table 10 Modified KME constitutive law parameters for 5083-H116

Parameter	Significance	Value	Source
M	Taylor factor	3.07	(Ryen et al. 2006)
α	Constant linking dislocation density to flow stress	0.3	(Verdier et al. 1998a)
b	Magnitude of Burger's vector	0.286 nm	
G	Shear modulus	26400 MPa	
L_0	Annihilation distance between two dislocations of opposite signh	16.6 nm	Mean value from 20°C/min tests (Summers et al. 2014)
K_{sg}	Efficiency of dislocation walls for dislocation annihilation	1030 nm	(Summers et al. 2014)
θ_0	Stage II hardening rate	5000 MPa	θ of 20°C/min tests in RX state

as spherical precipitates with an equivalent radius defined based on equivalent precipitate length. The PSD interaction and evolution during growth/dissolution were modeled using an Eulerian multi-class approach described by Perez, et al. (2008). The residual yield strength model uses PSD dependent solid solution and precipitate strengthening models. This section provides a summary of model development, including underlying assumptions as well as a description of basic model features. Refer to Summers (2014) for a detailed model description.

Residual yield strength model

A precipitate-dislocation interaction was developed to predict 6061-T651 residual yield strength. The KWN model is implemented to capture the yield strength evolution after non-isothermal thermal exposure.

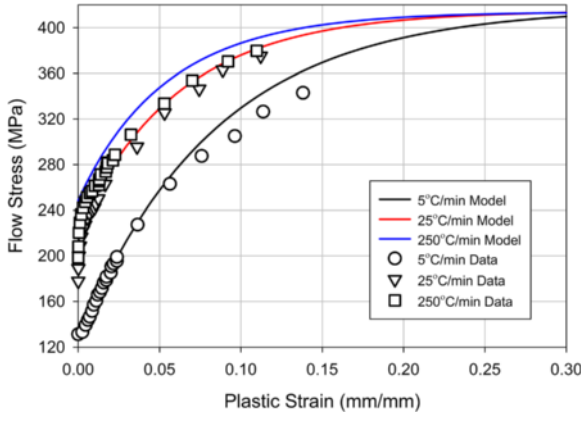

Figure 42 5083-H116 strain hardening after prior thermal exposure to 320°C at different heating rates as modeled using a modified KME constitutive law.

6061 residual yield strength is governed by the state of several microstructural strengthening contributions, specifically (i) the friction stress (σ_0), (ii) the solid solution content ($\Delta\sigma_{ss}$), (iii) precipitate contributions ($\Delta\sigma_p$), (iv) grain contributions (σ_g), and (v) dislocation forest hardening contributions (σ_g). These are linearly superposed to calculate the total yield strength (σ_y) as:

$$\sigma_y = \sigma_0 + \Delta\sigma_{ss} + \Delta\sigma_p + \sigma_g + \sigma_d \tag{25}$$

Linear superposition is assumed valid as the individual microstructural features strengthen the alloy at different length scales, thus negligible interaction is assumed. For 6061, the friction stress of pure aluminum is taken as the commonly accepted 10 MPa. The grain strengthening contribution (σ_g) is assumed negligible compared to that for solutes and precipitates. Dislocation forest hardening is given by the Taylor relation ($\sigma_d = M\alpha Gb\rho^{-1/2}$); however, σ_d is assumed to be much smaller than $\Delta\sigma_p$ and is thus ignored. Solid solution, $\Delta\sigma_{ss}$, and precipitate, $\Delta\sigma_p$, strengthening evolve due to precipitate nucleation, growth, and dissolution; the KWN model was implemented to account for these processes.

The non-isothermal yield strength model is given as

$$\sigma_y = \sigma_0 + H_{Mg_2Si}C_{Mg}^{2/3} + H_{Cu}C_{Cu}^{2/3} + \frac{M}{b}\left(2k_\Gamma Gb^2\right)^{-1/2}\sqrt{\frac{3f_v}{2\pi}}\frac{\bar{F}^{3/2}}{\bar{r}} \tag{26}$$

where the mean obstacle (precipitate) strength is given by $\bar{F}$. PSD evolution is implemented in the model as the Mg concentration in the matrix, C_{Mg}, mean precipitate radius, $\bar{r}$, precipitate volume fraction, f_v, and mean precipitate strength, $\bar{F}$. These parameters are a function of the PSD predicted by the KWN model. Refer to Summers (2014) for KWN model details and parameters. Model parameters are shown in Table 11.

The experimental evolution of yield strength after thermal exposure is well represented by model predictions in Figure 43. As expected, thermal exposures below 250°C do not cause a significant reduction in yield strength. Above 300°C, the yield strength decreases until precipitate and Mg aluminum matrix Mg content reaches an equilibrium state. The significant reduction in yield strength (~240 MPa reduction) is governed by significant precipitate growth and dissolution. The residual yield strength also depends on heating rate: the lower the heating rate, the lower the residual yield strength at a given maximum temperature. The effect of heating rate on yield strength is well captured by the model (Figure 43).

Residual strain hardening model

In the case of precipitation hardened alloys (e.g., 6061-T651), several models have been proposed to predict strain hardening behavior as a function of microstructure. Thermal exposure above ~250°C results in a transition from precipitate shearing by dislocations to Orowan looping (storage of a bypassing dislocation by pinning, bowing, and unpinning) due to precipitate growth. Several authors (Estrin 1996; Cheng et al. 2003; Poole and Lloyd 2004) considered the additional dislocation storage of Orowan loops through introduction of a term inversely proportional to precipitate spacing in the dislocation glide plane, which is effectively a function of precipitate volume fraction.

As discussed previously, aluminum alloy strain hardening is commonly modeled using the Kocks-Mecking-Estrin (KME) model (Mecking and Kocks 1981; Estrin and Mecking 1984; Hancock 1976; Kocks and Mecking 2003). Estrin (1996) generalized the KME model to include effects present in solute and precipitate hardened Al alloys. A new term was introduced to the KME formalism to account for Orowan loop storage around non-shearable precipitates. A similar modification was proposed by Barlat et al. (2002). Simar et al. (2007) adapted such an approach to model strain hardening of 6005A-T6 after thermal exposures such as those experienced during welding. A generalized form of the KME law is presented, focusing on the effects of Orowan loop storage stability on dislocation storage and dynamic recovery rates.

For 6061-T651, the KME relation in the Palm-Voce formalism is given as (Simar et al. 2007)

$$\frac{d\sigma}{d\varepsilon} = \theta - \beta(\sigma - \sigma_y) \tag{27}$$

where θ (MPa) and β (-) are apparent values for the dislocation storage rate and dynamic recovery used for commercial alloys, e.g., 6061-T651. θ and β are modified to include various microstructural effects as follows

- Orowan loop storage efficiency: ϕ is defined to include the effects of precipitate radius (i.e., the transition in precipitate-dislocation interaction from the age-hardened state to loss of coherency) on the dislocation storage rate, θ. The $(1/r)$ term in Eq. (28) is multiplied by ϕ.
- Dynamic precipitation: θ_{dp} is defined to include the effects of dynamic precipitation on the dislocation storage rate. The extent of dynamic precipitation during plastic deformation is dependent on the relative concentration of Mg in the Al matrix. θ is modified by linearly superposing θ_0 (i.e., the theoretical dislocation storage rate) and θ_{dp} in Eq. (28).
- Orowan loop storage: β is defined as a function of the probability of self-annihilating or encountering a stored dislocation (Orowan loop) during a given time interval. The mean number of precipitates encountered before two dislocations meet was determined using an assumed Poisson distribution.
- Yield strength effect on β: β_0 is defined as related to the material's yield strength with a theoretical minimum obtained for a material in super saturated solid solution with natural or artificial aging.

The expressions for θ and β in Eq. (27) are thus defined as

$$\frac{\theta}{G} = \frac{\theta_0 + \theta_{dp}}{2G} + \sqrt{\left(\frac{\theta_0}{2G}\right)^2 + \alpha^2 M^3 \beta \phi \left(\frac{b}{\bar{r}}\right) \sqrt{\frac{3f_v}{2\pi}}} \tag{28}$$

$$\beta = \beta_0 \exp\left(-\sqrt{\frac{3}{2\pi}} \frac{\sqrt{f_v} L_0 \phi}{\bar{r}}\right) + \frac{2y_p}{b}\left(1 - \exp\left(-\sqrt{\frac{3}{2\pi}} \frac{\sqrt{f_v} L_0 \phi}{\bar{r}}\right)\right) \tag{29}$$

The mean precipitate radius, $\bar{r}$, and volume fraction, f_v, are calculated using the PSD predicted by the KWN model (refer to Summers et al. (2014) for further details).

The generalized KME model dislocation storage rate, θ, and dynamic recovery rate, β, are detailed in Eqs. (28) and (29), respectively. Model parameters were identified through analysis using tensile mechanical tests of specimens previously heated at 20°C/min. The identification procedure is described in detail by Summers et al. (2014). All parameters of the KME model in the generalized relations for θ (Eq. (28)) and β (Eq. (29)) are provided in Table 12.

The modified KME model predictions are compared with experimental data (material heated at 5, 25, and 250°C/min to 350°C) in Figure 44. The temperature (350°C) was chosen as it coincides with significant PSD evolution. The tested heating rates span a large range of possible PSDs at this temperature. As is shown, the model shows good agreement with the experimental data. Note, somewhat competing effects of θ and β occur for 5°C/min ($\theta \approx 3600$ MPa, $\beta \approx 34$) and 25°C/min ($\theta \approx 3350$ MPa, $\beta \approx 31$). This results in a nearly identical prediction of strain hardening; however, the predicted strain hardening at both heating rates remains reasonable. Overall, the evolution in strain hardening behavior at different heating rates is well represented by the model.

Finite element predictions of residual mechanical behavior

The residual constitutive behavior characterized and modeled in the previous sections was extended to structural

Table 11 6061-T651 residual yield strength model parameters

Parameter	Significance	Value	Source
M	Taylor factor	2	Textured alloy (Simar et al. 2007)
G	Shear modulus	27 GPa	(Myhr and Grong 2000; Myhr et al. 2001; Myhr et al. 2004)
b	Magnitude of Burger's vector	0.286 nm	
σ_0	Friction stress of pure Al	10 MPa	(Myhr and Grong 2000; Myhr et al. 2001; Myhr et al. 2004)
H_{Cu}	Cu solid solution strengthening constant	46.4 MPa wt%$^{2/3}$	(Myhr and Grong 2000; Myhr et al. 2001; Myhr et al. 2004)
H_{Mg}	Mg solid solution strengthening constant	29.0 MPa wt%$^{2/3}$	(Myhr and Grong 2000; Myhr et al. 2001; Myhr et al. 2004)
H_{Si}	Si solid solution strengthening constant	66.3 MPa wt%$^{2/3}$	(Myhr and Grong 2000; Myhr et al. 2001; Myhr et al. 2004)
r_{trans}	Precipitate strength transition radius	3.044 nm	Mean radius of precipitates in PSD (Summers et al. 2014)
k_Γ	Line tension constant	0.40	σ_y in T6 state

sections and prior heating regimens which better represent that in a structural environment. The commercial finite element analysis package, Abaqus, was used to model the residual mechanical behavior of these sections.

Experiment

A series of small-scale thermostructural experiments was performed on 6061-T6 extruded square hollow sections. Sample geometries were 38.1 mm wide by 304.8 mm long with a 3.2 mm wall thickness. Similar to previous residual behavior experiments, these were conducted by thermally exposing the specimens, cooling to ambient conditions, then mechanically tested. Thermal exposures consisted of single-sided heating using a steel radiative plate followed immediately by water quenching. Two heat flux exposures were used – 50 and 70 kW/m^2. These exposures were selected as they resulted in steady-state exposed surface temperatures of about 350 and 400°C, respectively. Three exposure times were used – 300, 600, and 1200 s. Note, samples reached thermal equilibrium after about 600 s. The full-field temperatures of the sample side were measured during heating of each sample using a FLIR SC655 thermal infrared camera (640 × 480 pixels, 7.5 – 14 μm wavelength).

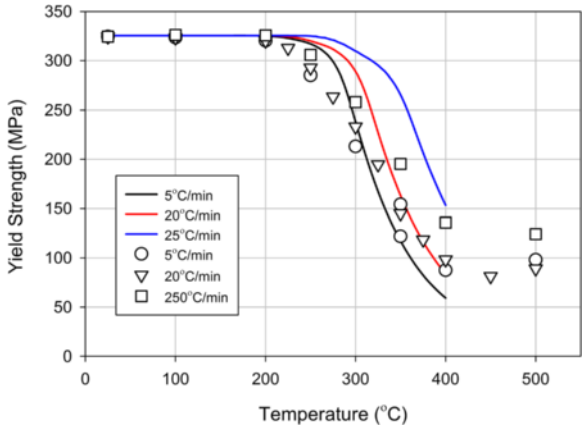

Figure 43 6061-T651 residual yield strength model predictions (lines) compared against experimental data (symbols).

After thermal exposure and water quenching, the square hollow sections were mechanically tested in four-point flexure. 10 mm diameter stainless steel rollers were used with an outer and inner roller spacing of 259 and 75 mm, respectively. All samples were oriented such that the inner span rollers applied load to the unexposed surface. This orientation was selected to simulate thermal exposure of the ceiling in compartment with loading from above.

FEA definition

The thermostructural experiments were modeled using the FEA package, Abaqus. Similar to the experiments, modeling was performed sequentially: a thermal model followed by a mechanical model. The thermal model includes the 6061 square hollow section and the steel radiant heater plate. The measured full-field temperatures of the steel plate heater were prescribed and the resultant full-specimen thermal response was predicted from the radiation exchange between the radiant heater and sample. Convective losses from the exterior surfaces were modeled based on isothermal vertical surfaces at 325°C. The convective heat transfer coefficient was calculated as 9 W/m^2-K using standard empirical correlations (Incropera et al. 2007).

Mechanical loading was modeled using a quasi-static displacement model sequentially coupled to the thermal model. The 10 mm rollers were included in the model. Mesh densities varied along the sample length with fine meshes at loading and support points. A simple hard contact model was used between the rollers (assumed a rigid body) and the sample. No tangential frictional forces were considered as forces were relatively low and a graphite-based lubricant was used in testing. Mechanical loading was modeled to a simulated cross-head displacement of 20 mm or when the model no longer converged. The reduced residual mechanical properties of the 6061 sample were input as that from Summers, et al. (2014) for linear heating rates of 5 and 25°C/min.

Table 12 Modified KME model parameters for 6061-T651

Parameter	Significance	Value	Source
θ_0	θ if no dynamic precipitation or Orowan loops	655 MPa	Minimum θ measured for all heating conditions
β_{min}	β at maximum σ_y	5.9	Minimum β measured for all heating conditions
$k_{\theta dp}$	Constant for θ_{dp} for dynamic precipitation effects	1210 MPa	θ for a solution heat treated sample and the AR material
σ_y^{max}	maximum yield strength (T6 state)	324 MPa	σ_y of as-received material
k_β	Constant linking σ_y to β	10.6	β for a solution heat treated sample and the AR material
r_{cl}	Equivalent radius of loss of coherency	8 nm	$\bar{r}$ of θ and β transition
L_0	Mean value of distance between two dislocations of opposite sign	42 nm	Modified Taylor hardening relation
a	Constant linking shear stress to dislocation density	0.15	Optimized from θ of 20°C/min samples
y_p	Annihilation distance when at least one precipitate exists between dislocations of opposite sign	13 nm	Optimized from β of 20°C/min samples

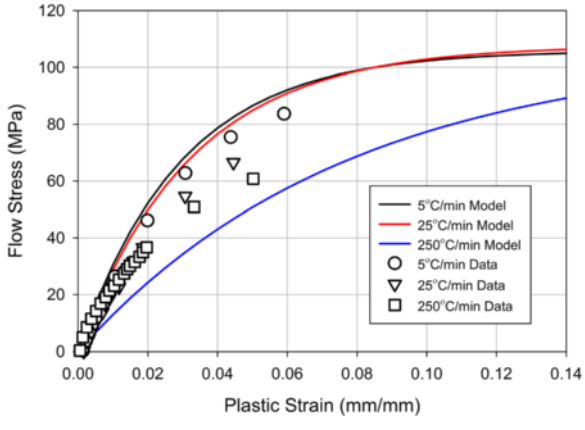

Figure 44 6061-T651 strain hardening after prior thermal exposure to 350°C at different heating rates as modeled using a modified KME constitutive law.

FEA results

A comparison of the measured full-field temperatures and those predicted by the thermal model is shown in Figure 45 for a 50 kW/m^2 heat flux. The thermal model captures the thermal gradient from the exposed to unexposed surface. For this exposure, the measured and predicted temperatures at all locations are generally within 10°C. For all tests, the left side is cooler due to non-uniformities in the radiant heater plate temperature. Comparison of the measured and predicted temperatures for the 70 kW/m^2 exposure is shown in Figure 46. The thermal model predicts temperatures within 5% of that measured; however, a larger amount of error exists towards the unexposed surface. This is possibly due to the assumed constant temperature (325°C) convection coefficient while these samples reach temperatures above 450°C on the exposed surface. Transient temperature measurements and predictions are also shown in Figure 47 for a location 3.2 mm from the exposed surface and at the mid-length. The model predicts the transient temperature response within 5% of experiment for both exposures.

FEA load-displacement predictions are compared against experiment in Figure 48 for the 50 kW/m^2 exposure. The mechanical model agrees well with the as-received sample mechanical response; however, the model tends to over-predict sample strength after prior thermal exposure. This may possibly be due to the slight discrepancy in material type used in property definitions (T651 plate) and these experiments (T6 extrusion). Despite this, the peak load is reasonably predicted for each test. The relationship between maximum exposure temperature and peak load is shown in Figure 49. Model predictions are shown for mechanical properties obtained after linear heating at 5 and 25°C/min (Summers, 2014). As expected, experiment shows decreasing peak load with increasing maximum exposure temperature. This is also reflected by model predictions. At 350°C, lower peak loads resulted from the 50 kW/m^2 exposure than at 70 kW/m^2. This is also as expected due to the time required to reach 350°C at the respective heat fluxes.

Summary

Aluminum alloys are increasingly being used in a broad spectrum of load-bearing applications such as lightweight structures, light rail, bridge decks, marine crafts, and off-shore platforms. A major concern in the design of land-based and marine aluminum structures is fire safety. In support of fire resistant structural design, an overview of 5083-H116 (strain hardened) and 6061-T651 (precipitation hardened) mechanical behavior both during and after fire was presented in this paper.

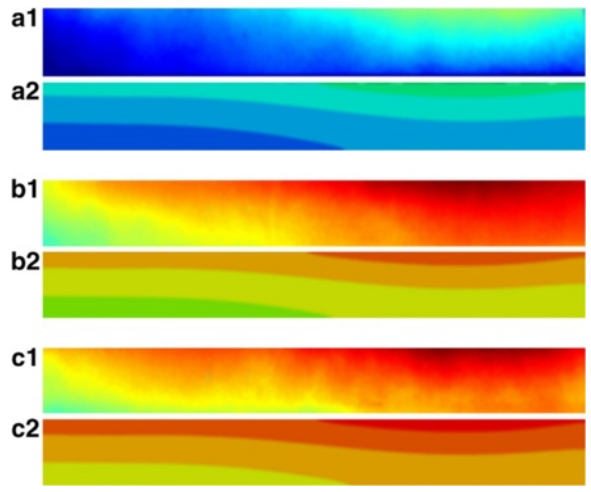

Figure 45 Measured and predicted maximum exposure temperatures for a 50 kW/m^2 exposure of a 6061 square hollow section for **(a)** 300 s, **(b)** 600 s, and **(c)** 1200 s.

The mechanical behavior during fire was characterized in terms of elevated temperature quasi-static tensile tests and creep tests. The Young's modulus was similar for both alloys. 5083-H116 had consistently lower yield strengths as compared to 6061-T651. Based on the reduction of area at fracture, 5083 as-received ductility is less than 6061; however, 5083 ductility increases more at elevated temperatures compared with 6061. For the alloys considered, the primary creep region is not significant except for 5083 at lower temperatures, i.e., less than 300°C. Thus, a modified Kachanov-Rabotnov creep model was presented to predict the accumulation of secondary and tertiary creep strains. The Larson-Miller parameter was implemented to predict creep rupture.

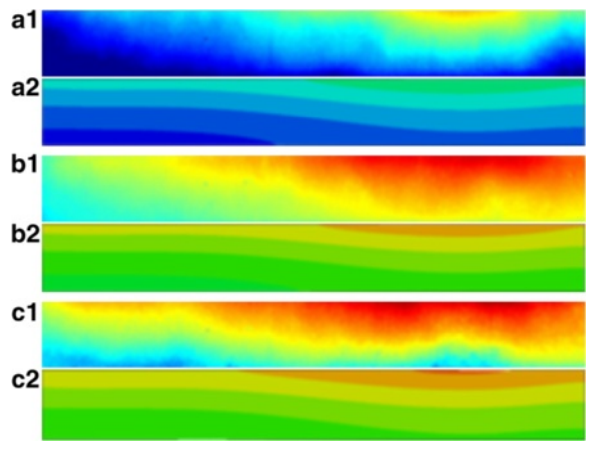

Figure 46 Measured and predicted maximum exposure temperatures for a 70 kW/m^2 exposure of a 6061 square hollow section for **(a)** 300 s, **(b)** 600 s, and **(c)** 1200 s.

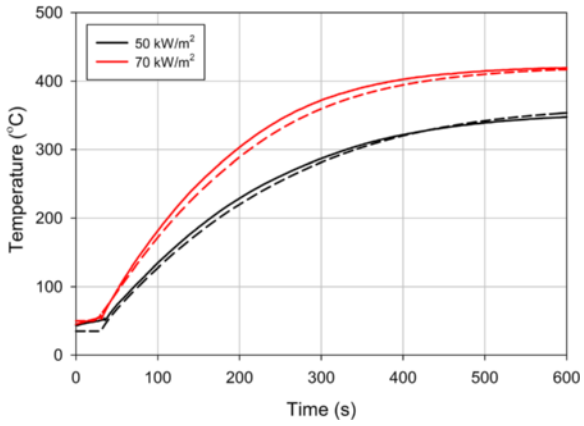

Figure 47 Measured (solid lines) and predicted (dashed lines) transient thermal response 3.2 mm from the exposed surface along the square hollow section mid-length.

The residual mechanical behavior after fire was characterized for materials previously exposed to thermal-only and thermomechanical conditions. Thermal exposure without applied stress causes microstructural evolution, i.e., dislocation recovery and recrystallization, resulting in strength reduction and significant changes in strain hardening. The Young's modulus negligibly changes following prior heating. 5083-H116 and 6061-T651 yield strength reduction is governed by microstructural evolution, which is time-temperature and maximum exposure temperature dependent. Thus, the temperature ranges over which strength degradation occurs in both alloys was measured to vary based on heating rate. If 5083 is heated to 400°C, the yield strength is reduced by 155 MPa (55%) from the as-received state with 36 MPa (13%) of the reduction attributed to recovery from 150 – 280°C and the remaining 116 MPa (42%) from 280 –

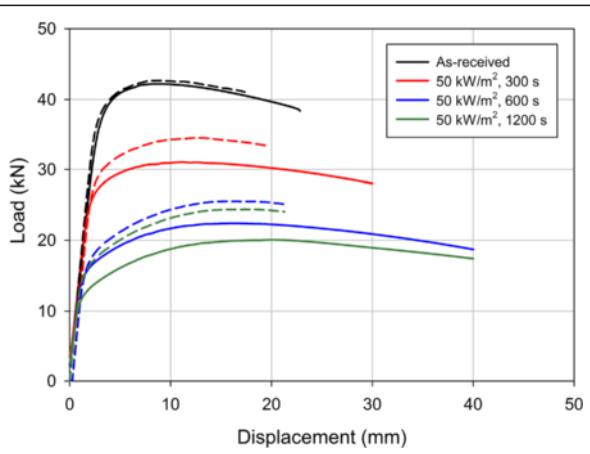

Figure 48 Measured (solid lines) and predicted (dashed lines) load-displacement response of 6061 square hollow section following prior thermal exposure at 50 kW/m^2.

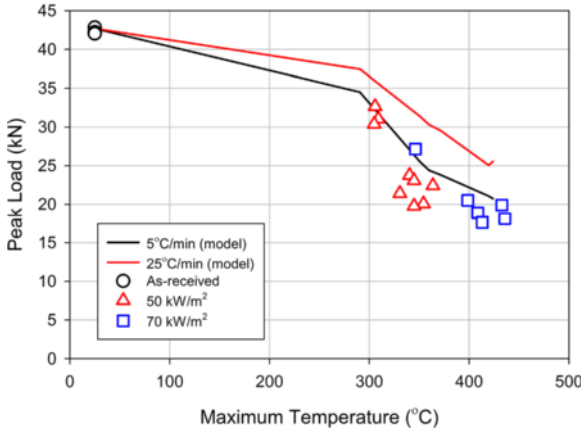

Figure 49 Relationship between peak load and maximum thermal exposure temperature of 6061 square hollow sections after prior thermal exposure at 50 and 70 kW/m^2. Model predictions (lines) are shown for mechanical properties after prior heating at 5 and 25°C/min (Summers et al. 2014).

360°C due to recrystallization. 6061-T651 yield strength reduces by 225 MPa after prior heating to 450°C with a steady decrease measured from 200 – 450°C due precipitate growth and dissolution. Thermomechanical exposure with applied stress results in dynamic microstructural evolution, primarily manifesting itself as cavitation development and grain elongation. These effects occur in both alloys; however, they are more prevalent in 5083 which experiences significantly higher creep strains as compared to 6061. 5083 also experiences dynamic recrystallization at high creep strains. The effects of cavitation (weakening) and grain elongation (strengthening) were generally not as significant as the strength reduction due to static microstructural evolution (i.e., 5083 – recovery, recrystallization; 6061 – precipitate growth and nucleation). Therefore, the effect of stress during prior thermal exposure was not determined to be significant in evaluating the residual constitutive behavior of aluminum alloys after fire exposure.

Models were presented for predicting the residual mechanical behavior of 5083-H116 and 6061-T651 aluminum alloys. These include simple empirical models including a conservative estimation method using a peak temperature or temperature history, microstructure-based constitutive models for residual mechanical behavior from a temperature history, and a finite element implementation. The appropriate model choice is dependent on the user's objectives such as the level of accuracy required.

Future research in this area should build on the uniaxial, static material constitutive behavior presented here. The following are areas that require investigation to develop a more detailed understanding of mechanical behavior of aluminum alloys during and following fires:

- Residual mechanical behavior of other aluminum alloys. This would include other 5xxx and 6xxx-series alloys, and the applicability of these other alloys to the models proposed herein. In addition, detailed investigations of other aluminum alloys (e.g., 2xxx or 7xxx-series) including microstructural investigation and its relation to mechanical behavior.
- Multi-axial material behavior at elevated temperature as well as residual mechanical behavior. Through this data, yield surfaces for the material can be obtained for a more general description of material response.
- Residual fatigue life following a fire exposure. This would provide expected life for materials subjected to cyclic loading, which is an important consideration in many transportation applications which commonly implement load-bearing aluminum components.
- Extension of the modified Kachanov-Rabotnov creep model to higher temperatures near the solidus temperature. Thus, the model would be able to predict burn-through in aluminum structures which is commonly responsible for fire spread to adjacent areas.

Competing interests
The authors declare that they have no competing interests.

Authors' contributions
PS performed the research on residual aluminum performance after fire including development of the microstructure-based models, performed the literature review, and drafted the manuscript. YC performed the research on the effect of thermomechanical damage and its effect on residual behavior. CR refined and further developed the creep model and performed the FEA research. BA performed the elevated temperature testing and initially developed the creep model. AM was involved in conceiving this work including oversight of its undertaking, he has also helped revise the manuscript. SC was involved in conceiving this work including oversight of its undertaking, he has also helped revise the manuscript. BL was involved in conceiving this work including oversight of its undertaking, he has also helped revise the manuscript and given its final approval. All authors have read and approved the final manuscript.

Acknowledgments
The authors would like to thank the Office of Naval Research, especially contract officers Dr. Stephen Turner and Dr. Louise Couchman for funding this research. The authors also acknowledge use of facilities within the Nanoscale Characterization and Fabrication Laboratory at Virginia Tech and the assistance of Dr. Chris Winkler. We also thank the help of many others during the course of this project including Emily Fogle, Ryan Matulich, Dr. Everson Kandare, and Dr. Stefanie Feih.

Author details
[1]Department of Mechanical Engineering, Virginia Tech, Blacksburg, VA 24061, USA. [2]Department of Engineering Science & Mechanics, Virginia Tech, Blacksburg, VA 24061, USA. [3]Department of Aerospace, Mechanical & Manufacturing Engineering, RMIT University, Melbourne, Australia.

Received: 2 October 2014 Accepted: 28 April 2015
Published online: 29 April 2015

References

Agarwal G, Lattimer B (2012) Method for measuring the standard heat of decomposition of materials. Thermochim Acta 545:34–47, doi:10.1016/j.tca.2012.06.027

AIME 135:416, Avrami M (1939) Kinetics of phase change. I: General theory. J Chem Phys 7:1103–1112
Allen B (2012) Thermomechanical behavior and creep response of marine-grade aluminum alloys. Thesis, Virginia Polytechnic Institute & State University
Amdahl J, Langhelle NK, Lundberg S (2001) Aluminium plated structures at elevated temperatures. Proc. OMAE 2001, Rio de Janeiro, Brazil
Anderson PM, Shewmon PG (2000) Stress redistribution and cavity nucleation near a diffusively growing grain boundary cavity. Mech Mater 32:175–191
Aouabdia Y, Boubertakh A, Hamamda S (2010) Precipitation kinetics of the hardening phase in two 6061 aluminium alloys. Mater Lett 64:353–356, doi:10.1016/j.matlet.2009.11.014
ASTM (2011) Standard E139, 2011: Standard test methods for conducting creep, creep-rupture, and stress-rupture tests of metallic materials. ASTM Interntaional, West Conshohocken, PA, doi:10.1520/E0139-11
ASTM Standard E1269 (2005) Standard test method for determining specific heat capacity by differential scanning calorimetry. ASTM International, West Conshohocken, PA, Doi:10.1520/E1269-11.2
ASTM Standard E1461 (2013) Standard test method for thermal diffusivity by the flash method. ASTM International, West Conshohocken, PA, doi:10.1520/E1461-13.2
ASTM Standard E21 (2009) Standard test methods for elevated temperature tension tests of metallic materials. ASTM International, West Conshohocken, PA, doi:10.1520/E0021-09.2
Bahrami A, Miroux A, Sietsma J (2012) An age-hardening model for Al-Mg-Si alloys considering needle-shaped precipitates. Metall Mater Trans A 43:4445–4453, doi:10.1007/s11661-012-1211-8
Bardel D, Perez M, Nelias D, Deschamps A, Hutchinson CR, Maisonnette D, Chaise T, Garnier J, Bourlier F (2014) Coupled precipitation and yield strength modelling for non-isothermal treatments of a 6061 aluminium alloy. Acta Mater 62:129–140, doi:10.1016/j.actamat.2013.09.041
Barlat F, Glazov MV, Brem JC, Lege DJ (2002) A simple model for dislocation behavior, strain and strain rate hardening evolution in deforming aluminum alloys. Int J Plast 18:919–939
Bay B, Hansen N (1979) Initial stages of recrystallization in aluminum of commercial purity. Metall Trans A 10:279–288
Bay B, Hansen N (1984) Recrystallization in commercially pure aluminum. Metall Trans A 15:287–297
Bratland DH, Grong Ø, Shercliff H, Myhr OR, Tjøtta S (1997) Modelling of precipitation reactions in industrial processing. Acta Mater 45:1–22
BSI (2007) BS EN 1999-1-2:2007. Eurocode 9 - Design of aluminum structures, Part 1-2: Structural fire design. BSI, London, UK
Bunge HJ, Wagner F, Welch PI, Van Houtte P (1985) A new way to include the grain shape in texture simulations with the Taylor model. J Phys Lett 46:1109–1113
Chen I-W (1983) Mechanisms of cavity growth in creep. Scr Metall 17:17–22
Chen Y (2014) Stress-induced damage and post-fire response of aluminum alloys. Dissertation, Virginia Polytechnic Institute & State University
Cheng LM, Poole WJ, Embury JD, Lloyd DJ (2003) The influence of precipitation on the work-hardening behavior of the aluminum alloys AA6111 and AA7030. Metall Mater Trans A 34:2473–2481
Clausen AH, Børvik T, Hopperstad OS, Benallal A (2004) Flow and fracture characteristics of aluminium alloy AA5083–H116 as function of strain rate, temperature and triaxiality. Mater Sci Eng A 364:260–272, doi:10.1016/j.msea.2003.08.027
Cocks ACF, Ashby MF (1982) Creep fracture by coupled power-law creep and diffusion under multiaxial stress. Met Sci 16:465–474
Courtney TH (2000) Mechanical behavior of materials. McGraw-Hill, New York
Deschamps A, Bréchet Y (1998) Influence of predeformation and ageing of an Al–Zn–Mg alloy—II. Modeling of precipitation kinetics and yield stress. Acta Mater 47:293–305, doi:10.1016/S1359-6454(98)00296-1
Deschamps A, Niewczas M, Bley F, Bréchet Y, Embury JD, Le Sinq L, Livet F, Simon JP (1999) Low-temperature dynamic precipitation in a supersaturated Al-Zn-Mg alloy and related strain hardening. Philos Mag A 79:2485–2504
Dieter G (1976) Mechanical metallurgy, 2nd edn. McGraw-Hill, New York
Doan LC, Ohmori Y, Nakai K (2000) Precipitation and dissolution reactions in a 6061 aluminum alloy. JIM, Mater Trans 41:300–305
Doherty RD, Hughes DA, Humphreys FJ, Jonas JJ, Juul Jensen D, Kassner ME, King ME, McNelley TR, McQueen HJ, Rollet AD (1997) Current issues in recrystallization: a review. Mater Sci Eng A 238:219–274, doi:10.1016/S0921-5093(97)00424-3
Edwards GA, Stiller K, Dunlop GL, Couper MJ (1998) The precipitation sequence in Al-Mg-Si alloys. Acta Mater 46:3893–3904, doi:10.1016/S1359-6454(98)00059-7
El-Danaf EA, AlMajid AA, Soliman MS (2008) Hot deformation of AA6082-T4 aluminum alloy. J Mater Sci 43:6324–6330, doi:10.1007/s10853-008-2895-4
Esmaeili S, Lloyd DJ (2005) Characterization of the evolution of the volume fraction of precipitates in aged AlMgSiCu alloys using DSC technique. Mater Charact 55:307–319, doi:10.1016/j.matchar.2005.07.007
Estrin Y (1996) Dislocation-density-related constitutive modeling. In: Krausz A, Krausz K (eds) Unified constitutive laws of plastic deformation. Academic Press, San Diego, pp 9–106
Estrin Y, Mecking H (1984) A unified phenomenological description of work hardening and creep based on one-parameter models. Acta Metall 32:57–70
Evans HE (1984) Mechanisms of creep fracture. Elsevier Applied Science, London
Faggiano B, De Matteis G, Landolfo R, Mazzolani FM (2004) Behaviour of aluminium alloy structures under fire. J Civ Eng Manag 10:183–190
Fujita H, Tabata T (1973) The effect of grain size and deformation sub-structure on mechanical properties of polycrystalline aluminum. Acta Metall 21:355–365
Furu T, Ørsund R, Nes E (1995) Subgrain growth in heavily deformed aluminium—experimental investigation and modelling treatment. Acta Metall Mater 43:2209–2232
Gaber A, Gaffar MA, Mostafa MS, Abo Zeid AF (2006) Investigation of developed precipitates in Al–1·1 wt-%Mg2Si balanced alloy by DSC and SEM techniques. Mater Sci Technol 22:1483–1488, doi:10.1179/174328406X100707
Gallais C, Simar A, Fabregue D, Denquin A, Lapasset G, de Meester B, Brechet Y, Pardoen T (2007) Multiscale analysis of the strength and ductility of AA 6056 aluminum friction stir welds. Metall Mater Trans A 38:964–981, doi:10.1007/s11661-007-9121-x
Gallais C, Denquin A, Bréchet Y, Lapasset G (2008) Precipitation microstructures in an AA6056 aluminium alloy after friction stir welding: Characterisation and modelling. Mater Sci Eng A 496:77–89, doi:10.1016/j.msea.2008.06.033
Goods SF, Nix WD (1978) The kinetics of cavity growth and creep fracture in silver containing implanted grain boundary cavities. Acta Metall 26:739–752
Greenwood JN, Miller DR, Suiter JW (1954) Intergranular cavitation in stressed metals. Acta Metall 2:250–258
Grong Ø, Shercliff HR (2002) Microstructural modelling in metals processing. Prog Mater Sci 47:4–9
Gupta AK, Lloyd DJ, Court SA (2001) Precipitation hardening processes in an Al–0.4% Mg–1.3% Si–0.25% Fe aluminum alloy. Mater Sci Eng A 301:140–146
Hancock JW (1976) Creep cavitation without a vacancy flux. Met Sci 10:319–325
Hasegawa T, Kocks UF (1979) Thermal recovery processes in deformed aluminum. Acta Metall 27:1705–1716
Huang Y, Humphreys FJ (1999) Measurements of grain boundary mobility during recrystallization of a single-phase aluminium alloy. Acta Mater 47:2259–2268, doi:10.1016/S1359-6454(99)00062-2
Huang Y, Humphreys FJ (2012) The effect of solutes on grain boundary mobility during recrystallization and grain growth in some single-phase aluminium alloys. Mater Chem Phys 132:166–174, doi:10.1016/j.matchemphys.2011.11.018
Hulla D, Rimmera DE (1959) The growth of grain-boundary voids under stress. Philos Mag A 4:673–687
Huskins EL, Cao B, Ramesh KT (2010) Strengthening mechanisms in an Al–Mg alloy. Mater Sci Eng A 527:1292–1298, doi:10.1016/j.msea.2009.11.056
Incropera FP, DeWitt DP, Bergman TL, Lavine AS (2007) Fundamentals of heat and mass transfer, 6th edn. John Wiley & Sons, Hoboken, NJ
Johnson WA, Mehl R (1939) Reaction kinetics in processes of nucleation and growth. Trans AIME 135:416
Jones AR, Ralph B, Hansen N (1979) Subgrain coalescence and the nucleation of recrystallization at grain boundaries in aluminium. Proc R Soc London A 368:345–357
Kachanov LM (1999) Rupture time under creep conditions. Int J Fract 97:11–18
Kampmann R, Wagner R (1984) Kinetics of precipitation in metastable binary alloys – theory and application to Cu-1.9 at% Ti and Ni-14 at% Al. In: Decompositions of alloys: the early stages. Pergamon Press, Oxford, UK, pp 91–103
Kandare E, Feih S, Lattimer BY, Mouritz AP (2010) Larson–Miller failure modeling of aluminum in fire. Metall Mater Trans A 41:3091–3099, doi:10.1007/s11661-010-0369-1
Kassner ME, Hayes TA (2003) Creep cavitation in metals. Int J Plast 19:1715–1748, doi:10.1016/S0749-6419(02)00111-0
Kaufman JG (ed) (2000) Introduction to aluminum alloys and tempers. ASM International, Metals Park, OH

Khan IN, Starink MJ, Yan JL (2008) A model for precipitation kinetics and strengthening in Al–Cu–Mg alloys. Mater Sci Eng A 472:66–74, doi:10.1016/j.msea.2007.03.033
Kocks UF (1976) Laws for work-hardening and low-temperature creep. J Eng Mater Technol 76–85
Kocks UF, Mecking H (2003) Physics and phenomenology of strain hardening: the FCC case. Prog Mater Sci 48:171–273, doi:10.1016/S0079-6425(02)00003-8
Kolmogorov AN (1937) A statistical theory for the recrystallization of metals. Izv Akad Nauk SSSR 3:355
Konopleva EV, McQueen HJ, Evangelista E (1995) Serrated grain boundaries in hot-worked aluminum alloys at high strains. Mater Charact 5803:251–264
Langhelle NK (1996) Buckling tests of aluminium columns at elevated temperatures. Proc Int Conf Offshore Mech Arct Eng - OMAE 2:387–394
Langhelle NK, Amdahl J (2001) Experimental and numerical analysis of aluminium columns subjected to fire. In: Proc. 11th Int. Offshore Polar Eng. Conf., Stavenger, Norway, 17-22 June, 2001
Larson F (1952) A time-temperature relationship for rupture and creep stresses. Am Soc Mech Eng Trans 74:765–771
Last HR, Garrett RK (1996) Mechanical behavior and properties of mechanically alloyed aluminum alloys. Metall Mater Trans A 27:737–745, doi:10.1007/BF02648961
Leckie FA, Hayhurst DR (1974) Creep rupture of structures. Proc R Soc A Math Phys Eng Sci 340:323–347, doi:10.1098/rspa.1974.0155
Lin J, Liu Y, Dean TA (2005) A review on damage mechanisms, models and calibration methods under various deformation conditions. Int J Damage Mech 14:299–319, doi:10.1177/1056789505050357
Liu R, Salahshoor M, Melkote SN, Marusich T (2014) A unified internal state variable material model for inelastic deformation and microstructure evolution in SS304. Mater Sci Eng A 594:352–363, doi:10.1016/j.msea.2013.11.071
Maisonnette D, Suery M, Nelias D, Chaudet P, Epicier T (2011) Effects of heat treatments on the microstructure and mechanical properties of a 6061 aluminium alloy. Mater Sci Eng A 528:2718–2724, doi:10.1016/j.msea.2010.12.011
Maljaars J, Fellinger J, Soetens F (2005) Fire exposed aluminium structures. HERON 50:261–278
Maljaars J, Soetens F, Katgerman L (2008) Constitutive model for aluminum alloys exposed to fire conditions. Metall Mater Trans A 39:778–789, doi:10.1007/s11661-008-9470-0
Maljaars J, Soetens F, Snijder HH (2009a) Local buckling of aluminium structures exposed to fire. Part 1: Tests. Thin-Walled Struct 47:1404–1417, doi:10.1016/j.tws.2009.02.008
Maljaars J, Soetens F, Snijder HH (2009b) Local buckling of aluminium structures exposed to firePart 2: Finite element models. Thin-Walled Struct 47:1418–1428, doi:10.1016/j.tws.2008.06.003
Matulich RD (2011) Post-fire mechanical properties of aluminum alloys and aluminum welds. Thesis, Virginia Polytechnic Institute & State University
Mazzolani FM (1995) Aluminum alloy structures, 2nd edn. E & FN Spon imprint of Chapman & Hall, London, UK
McQueen HJ, Ryum N (1985) Hot working and subsequent static recrystallization of Al and Al-Mg alloys. Scand J Metall 14:183–194
Mecking H, Kocks UF (1981) Kinetics of flow and strain-hardening. Acta Metall 29:1865–1875
Myhr OR, Grong Ø (1991a) Process modelling applied to 6082-T6 aluminium weldments–I. Reaction kinetics. Acta Metall 39:2693–2702
Myhr OR, Grong Ø (1991b) Process modelling applied to 6082-T6 aluminium weldments—II. Applications of model. Acta Metall Mater 39:2703–2708
Myhr OR, Grong Ø (2000) Modelling of non-isothermal transformations in alloys containing a particle distribution. Acta Mater 48:1605–1615, doi:10.1016/S1359-6454(99)00435-8
Myhr OR, Grong Ø, Andersen SJ (2001) Modelling of the age hardening behaviour of Al-Mg-Si alloys. Acta Mater 49:65–75
Myhr OR, Grong Ø, Klokkehaug S, Fjaer HG (2002) Modelling of the microstructure and strength evolution during ageing and welding of Al–Mg–Si alloys. In: Cerjak H (ed) Mathematical modeling of weld phenomena, vol 6. Maney, London, UK
Myhr OR, Grong Ø, Fjær HG, Marioara CD (2004) Modelling of the microstructure and strength evolution in Al-Mg-Si alloys during multistage thermal processing. Acta Mater 52:4997–5008, doi:10.1016/j.actamat.2004.07.002
Nicolas M, Deschamps A (2003) Characterisation and modelling of precipitate evolution in an Al–Zn–Mg alloy during non-isothermal heat treatments. Acta Mater 51:6077–6094, doi:10.1016/S1359-6454(03)00429-4
Perez M, Dumont M, Acevedo-Reyes D (2008) Implementation of classical nucleation and growth theories for precipitation. Acta Mater 56:2119–2132, doi:10.1016/j.actamat.2007.12.050
Poole WJ, Lloyd DJ (2004) Modelling the stress-strain behaviour for aluminum alloy AA6111. In: Proceeding 9th Int. Conf. Alum. Alloys, Brisbane, Australia, 2-5 August 2004
Popović M, Romhanji E (2008) Characterization of microstructural changes in an Al-6.8wt.% Mg alloy by electrical resistivity measurements. Mater Sci Eng A 492:460–467, doi:10.1016/j.msea.2008.04.001
Rabotnov YN (1969) Creep problems in structural members. North-Holland, Amsterdam
Raj R, Ashby MF (1975) Intergranular fracture at elevated temperature. Acta Metall 23:653–666
Ryen Ø, Nijs O, Sjölander E, Holmedal B, Ekström H-E, Nes E (2006) Strengthening mechanisms in solid solution aluminum alloys. Metall Mater Trans A 37:1999–2006
Simar A, Bréchet Y, de Meester B, Denquin A, Pardoen T (2007) Sequential modeling of local precipitation, strength and strain hardening in friction stir welds of an aluminum alloy 6005A-T6. Acta Mater 55:6133–6143, doi:10.1016/j.actamat.2007.07.012
Simar A, Bréchet Y, de Meester B, Denquin A, Pardoen T (2008) Microstructure, local and global mechanical properties of friction stir welds in aluminium alloy 6005A-T6. Mater Sci Eng A 486:85–95, doi:10.1016/j.msea.2007.08.041
Summers PT (2014) Microstructure-based constitutive models for residual mechanical behavior of aluminum alloys after fire exposure. Dissertation, Virginia Polytechnic Institute & State University
Summers PT, Matulich RD, Case SW, Lattimer B (2012) Post-fire mechanical properties and hardness of 5083 and 6082 aluminum alloys. ASME IMECE 2012, Houston, USA
Summers PT, Case SW, Lattimer BY (2014) Residual mechanical properties of aluminum alloys AA5083-H116 and AA6061-T651 after fire. Eng Struct 76:49–61
Sun S, Sundararaghavan V (2012) A probabilistic crystal plasticity model for modeling grain shape effects based on slip geometry. Acta Mater 60:5233–5244, doi:10.1016/j.actamat.2012.05.039
Suzuki J, Ohmiya Y, Wakamatsu T, Haradaz K, Yusa S, Kohno M (2005) Evaluation of fire resistance of aluminum alloy members. Fire Sci Technol 24:237–255
Trinkaus H, Yoo MH (1987) Nucleation under time-dependent supersaturation. Philos Mag A 55:269–289
Underwriter Laboratories (1990) Rapid rise fire tests of protection materials for structural steel. ANSI/UL 1709, Northbrook, IL
Vandermeer RA, Hansen N (2008) Recovery kinetics of nanostructured aluminum: Model and experiment. Acta Mater 56:5719–5727, doi:10.1016/j.actamat.2008.07.038
Vandermeer RA, Juul Jensen D (1994) Modeling microstructural evolution of multiple texture components during recrystallization. Acta Metall Mater 42:2427–2436, doi:10.1016/0956-7151(94)90321-2
Vandermeer RA, Juul Jensen D (2001) Microstructural path and temperature dependence of recrystallization in commercial aluminum. Acta Mater 49:2083–2094, doi:10.1016/S1359-6454(01)00074-X
Vandermeer RA, Rath BB (1990) Interface migration during recrystallization: the role of recovery and stored energy gradients. Metall Trans A 21:1143–1149
Verdier M, Brechet Y, Guyot P (1998a) Recovery of AlMg alloys: flow stress and strain-hardening properties. Acta Mater 47:127–134
Verdier M, Janecek M, Bréchet Y, Guyot P (1998b) Microstructural evolution during recovery in Al–2.5% Mg alloys. Mater Sci Eng A 248:187–197
Wen W, Morris JG (2003) An investigation of serrated yielding in 5000 series aluminum alloys. Mater Sci Eng A 354:279–285, doi:10.1016/S0921-5093(03)00017-0
Xing Q, Huang X, Hansen N (2006) Recovery of heavily cold-rolled aluminum: Effect of local texture. Metall Mater Trans A 37:1311–1322
Yoo MH, Trinkaus H (1986) Interaction of slip with grain boundary and its role in cavity nucleation. Acta Metall 34:2381–2390